# Inverse exchange bias effects and magnetoelectric coupling of the half-doped perovskite-type chromites $Gd_{0.5}Sr_{0.5}CrO_3$ and $Gd_{0.5}Ca_{0.5}CrO_3$

Biswajit Dalal [1,*] Xun Kang,[1,2] Yoshitaka Matsushita,[3] Alexei A. Belik [1]
Yoshihiro Tsujimoto [1,2] and Kazunari Yamaura [1,2,†]

[1]*International Center for Materials Nanoarchitectonics (WPI-MANA), National Institute for Materials Science,*
*Namiki 1-1, Tsukuba, Ibaraki 305-0044, Japan*
[2]*Graduate School of Chemical Sciences and Engineering, Hokkaido University,*
*North 10 West 8, Kita-ku, Sapporo, Hokkaido 060-0810, Japan*
[3]*Materials Analysis Station, National Institute for Materials Science, 1-2-1 Sengen, Tsukuba, Ibaraki 305-0047, Japan*

The $Cr^{4+}$ oxidation state with two electrons in the Cr $3d$ shell is not often observed in perovskite-type oxides, as high pressures and temperatures are generally required to stabilize the octahedral coordination. Herein, we present a comparative study of the half-doped perovskite-type chromites $Gd_{0.5}Sr_{0.5}CrO_3$ (GSCO) and $Gd_{0.5}Ca_{0.5}CrO_3$ (GCCO). Fifty percent of the Cr occurs in the $Cr^{4+}$ oxidation state after high-pressure synthesis at 6 GPa and 1200 °C. The materials were investigated using synchrotron x-ray diffraction, magnetization, heat capacity, and dielectric measurements. The diffraction patterns show that GSCO and GCCO crystallize in orthorhombic (*Pnma*) structures with different degrees of local lattice distortion. GSCO exhibits a long-range magnetic order at temperatures of $< 98$ K, accompanied by magnetization reversal, suggesting that the magnetic ground state is ferrimagnetic. In contrast, GCCO displays antiferromagnetic characters at temperatures $<\sim 100$ K. In addition, GSCO exhibits a crossover between conventional and inverse exchange bias effects at low temperatures ($< 50$ K). This is likely caused by asymmetric exchange Dzyaloshinskii-Moriya interactions between the Cr ions of different valences ($+3$ and $+4$). Furthermore, significant magnetoelectric coupling at the onset of the magnetic order is supported by temperature-dependent dielectric measurements.

DOI: [10.1103/PhysRevB.106.104425](10.1103/PhysRevB.106.104425)

## I. INTRODUCTION

Perovskite-type orthochromite $R$CrO$_3$, where $R$ is a rare-earth element, receives considerable attention owing to its potential applications and unique physical properties, such as negative magnetization, temperature- and field-induced fast spin switching, spin reorientation, field-induced switchable polarization, magnetoelectric effects, spin-driven ferroelectricity, magnetoelastic coupling, and exchange bias (EB) and giant magnetocaloric effects [1–14]. Most orthochromites crystallize in perovskite-type orthorhombic structures (space groups of *Pnma* or *Pbnm*) and exhibit canted antiferromagnetic (AFM) orders. An antisymmetric exchange Dzyaloshinskii-Moriya (DM) interaction causes a weak ferromagnetic (FM) component between the $Cr^{3+}$ spins to manifest at temperatures below the AFM transition (Néel) temperature ($T_N$) [15,16]. Superexchange interactions through the $Cr^{3+}$–O–$Cr^{3+}$ bond likely cause the AFM order, and complex, anisotropic interactions between $R^{3+}$ and $Cr^{3+}$ may cause unusual physical phenomena, e.g., the polar order of $R$CrO$_3$ may be primarily caused by $R$–Cr exchange striction (i.e., an exchange field between the $R$ ion and Cr sublattice) [6].

Furthermore, the onset temperatures of spin-driven ferroelectricity and long-range AFM order of all $R$CrO$_3$ remain within the range 110–290 K, regardless of the ionic radius of $R^{3+}$ [7,12].

GdCrO$_3$ undergoes a canted AFM transition at a $T_N$ of 167 K, with negative magnetization, spin reorientation, and field-induced polar order. These complex features are likely caused by interactions between two magnetic elements, $Gd^{3+}$ ($4f^7$) and $Cr^{3+}$ ($3d^3$) [2,5,6]. In addition, spontaneous spin reorientation of the ordered Cr sublattice occurs at 7 K [2,5]. The DM interactions and strong AFM coupling between Gd moments and Cr sublattices may lead to negative magnetization at a specific compensation temperature ($T_{comp}$). Recently, an unusual EB effect and fast spin switching were observed in single-crystal GdCrO$_3$ [17], which exhibited a giant magnetocaloric effect and temperature-induced magnetization jump [18,19]. Owing to these multiple anomalies, additional studies of GdCrO$_3$ are required to clarify its fundamental nature.

Half-doped perovskite-type transition metal oxides, such as manganite and cobaltite, were extensively investigated over recent decades owing to their strong intercorrelations among various characteristics—spin, charge, orbital, and lattice [20–24]. Studies of half-doped manganite (La$_{0.5}$Ca$_{0.5}$MnO$_3$) were conducted by Wollan and Koehler [25] and Goodenough [26]. The charge-exchanged AFM ground state was associated with the spatial order of the $Mn^{3+}$/$Mn^{4+}$ ions localized

*b.dalal.iitd@gmail.com
†YAMAURA.kazunari@nims.go.jp

in alternate planes. The most notable discovery to date is the colossal magnetoresistance of mixed-valence manganite $Pr_{0.5}Sr_{0.5}MnO_3$ [27], with significant competition between the FM metal and AFM insulator states [28]. Notably, however, there are contradictory reports regarding the origin of the colossal magnetoresistance [29–33].

In addition, half-doped manganites exhibit various phenomena, including double-exchange ferromagnetism, metal-insulator transitions, Griffiths phases, charge-order-driven ferroelectricity, strong magnetoelectric coupling, magnetodi-electric and EB effects, and magnetoelectric phase separation [34–44]. Conversely, half-doped cobaltites exhibit unconventional phase transitions and unexpected properties, such as spin-state transitions, spin reorientations, valence-state and photoinduced metal-insulator transitions, and charge transfer [45–52].

The syntheses of half-doped manganites and cobaltites with perovskite structures and $Mn^{4+}$ and $Co^{4+}$ in octahedral coordination yield compounds with unprecedented physical properties. However, the synthesis of half-doped chromite receives less attention, likely because high pressures and temperatures are required to stabilize $Cr^{4+}$ in octahedral coordination within the perovskite-type structure. We thus investigated $Gd_{0.5}A_{0.5}CrO_3$, where $A = Sr$ or $Ca$, using a high-pressure and high-temperature method, as half-doped alkaline-earth metal ions could cause distinct electrical transport and magnetic phenomena, such as, semiconducting and ferrimagnetic (FiM) ground state, magnetic frustration associated with competing AFM and FiM/FM interactions, magnetostriction, inverse EB effect, and magnetoelectric coupling accompanying with the ferroelectric relaxorlike state.

In this paper, we reveal the magnetic and electric properties of two half-doped chromites, $Gd_{0.5}Sr_{0.5}CrO_3$ (GSCO) and $Gd_{0.5}Ca_{0.5}CrO_3$ (GCCO), which were synthesized at 6 GPa and 1200 °C. GSCO exhibited a FiM ground state, whereas GCCO exhibited an AFM ground state. In addition, GSCO exhibited magnetization reversal, non-Griffith-like clustered FM features at temperatures of $> T_{FiM}$ (FiM transition temperature), and inverse EB effects. Furthermore, temperature-dependent permittivity studies revealed magnetoelectric coupling in GSCO and GCCO.

## II. EXPERIMENTAL DETAILS

Polycrystalline GSCO and GCCO were synthesized via a solid-state reaction using powders of $Gd_2O_3$, SrO (prepared using $SrCO_3$ by heating at 1300 °C in oxygen), CaO (prepared using $CaCO_3$ by heating at 1300 °C in oxygen), $Cr_2O_3$, and $CrO_2$. The powders were thoroughly mixed in an agate mortar in a stoichiometric ratio in an Ar-filled glovebox. Each mixture was sealed in a Pt capsule and loaded into a multi-anvil press (CTF-MA1500P, C&T Factory, Tokyo, Japan), and the capsule was compressed statically and isotropically at a pressure of 6 GPa at 1200 °C for 1 h (temperature ramping required 12 min). After heating, the capsule was quenched to a temperature of $< 100$ °C within 1 min, and the pressure was gradually released over several hours. The resulting material was a dense, polycrystalline, black pellet. A sample was finely ground for use in phase identification using a MiniFlex600

x-ray diffractometer (Rigaku, Tokyo, Japan) with Cu $K_\alpha$ radiation.

Finely ground powders were used in synchrotron x-ray diffraction (XRD) at temperatures between 120 and 750 K using a large Debye-Scherrer camera at the BL15XU beam-line at SPring-8, Sayo, Japan [53,54]. The wavelength of the synchrotron XRD was 0.65297 Å, calibrated using a standard material $CeO_2$. Synchrotron XRD data were analyzed via the Rietveld method [55] using RIETAN-FP [56] and MAUD software [57]. Crystal structure was drawn using VESTA software [58].

The direct current (dc) magnetic susceptibilities ($\chi$) of the materials were measured using a superconducting quantum interference device magnetometer (MPMS, Quantum Design, San Diego, CA, USA). To correct for the stray magnetic field of the superconducting magnet, the magnet was degaussed before each measurement. Measurements were conducted in the temperature range 2–350 K at various applied magnetic fields ($H$) under zero-field-cooled (ZFC) and field-cooled (FC) conditions. Isothermal magnetization loops were collected at various temperatures in the magnetic field range $\pm 70$ kOe. The alternating current (ac) $\chi$ of GSCO was measured at 5–350 K using the same instrument. The reproducibility of GSCO and GCCO magnetic data was verified using a set of materials prepared in different high-pressure runs.

The electrical resistivity ($\rho$) of a polycrystalline material was measured as a function of temperature via a 4-probe method using a physical property measurement system (PPMS, Quantum Design). The electrical contacts on the bar-shaped material comprised Au wires and Ag epoxy. The temperature-dependent specific heat capacity ($C_{total}$) was measured using a thermal relaxation method under a zero field or an applied field of 90 kOe in the PPMS at temperatures of 2–300 K. We used an Apiezon-N grease to thermally connect the material to the holder stage.

The dielectric properties were measured at temperatures of 5–300 K using an Alpha-A high-performance frequency analyzer (Novocontrol Technologies, Montabaur, Germany) in the frequency range 100 Hz–2 MHz at $H = 0$ or 90 kOe in the PPMS. During the measurement of GSCO, an extrinsic contribution to the dielectric constant was observed between 220 and 270 K, which was likely due to ice. However, the extrinsic contribution was no longer observed under a much higher vacuum [59]. The deviation between the material and system temperatures under a high vacuum became significant at $< 50$ K. Therefore, we combined the data measured under normal and high-vacuum conditions to confirm the dielectric behavior of the material.

## III. RESULTS AND DISCUSSION

### A. Crystal structure

The crystal structures of GSCO and GCCO at room temperature ($\sim 297$ K) were investigated via synchrotron XRD and data analysis using the Rietveld method, as shown in Figs. 1(a) and 1(b), respectively. Based on the structure of $RCrO_3$ at room temperature, we initially refined the crystal structure of GSCO using a distorted orthorhombic model (*Pbnm* or its axial transformed standard setting *Pnma*, No.
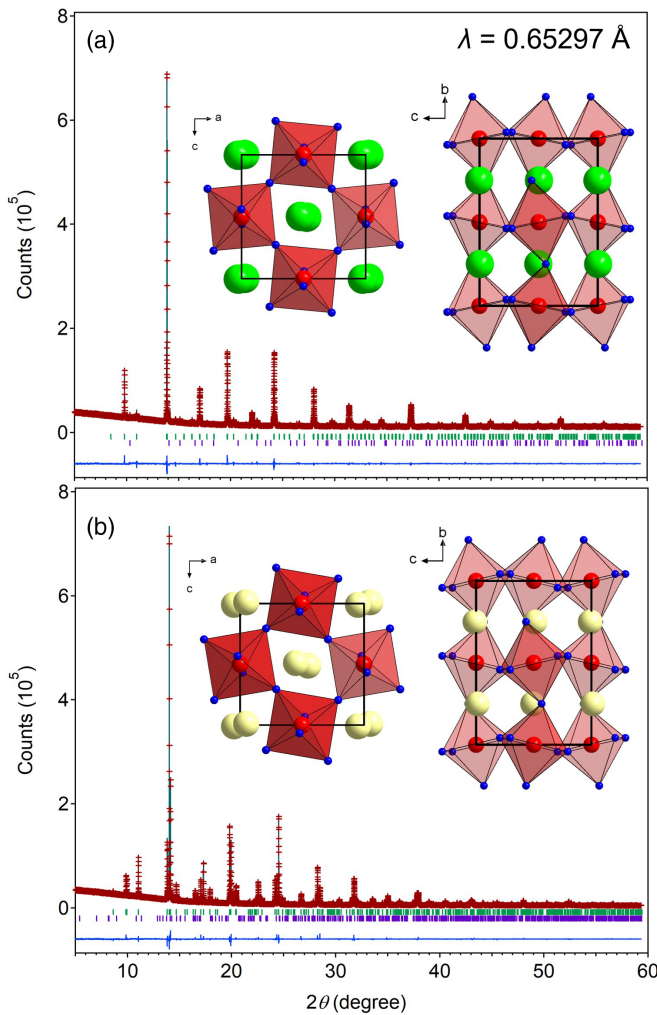
FIG. 1. Rietveld refinement of the synchrotron x-ray diffraction (XRD) patterns of (a) GSCO and (b) GCCO collected at room temperature. The crosses and solid red lines represent the observed and calculated patterns, respectively, with the differences (solid blue lines) shown at the bottom. The vertical ticks indicate the positions of the allowed Bragg reflections. The upper (olive) and bottom (magenta) rows indicate the reflections of the main and secondary phases, respectively. The lattice parameters are $a = 5.41289(2)$ Å, $b = 7.63652(2)$ Å, and $c = 5.39966(2)$ Å for GSCO ($Pnma$), and $a = 5.42543(1)$ Å, $b = 7.54252(1)$ Å, and $c = 5.31059(1)$ Å for GCCO ($Pnma$). The secondary phase is $Cr_2O_3$ (1.7 wt. %) for GSCO and $CaCr_2O_4$ (2.5 wt. %) for GCCO. The unit cell of each material is shown as an inset. Green, yellow, blue, and red balls denote Gd/Sr, Gd/Ca, O, and Cr, respectively.

62) and a cubic $Pm-3m$ model (No. 221). Additionally, we tested a monoclinic $P2_1/c$ model (No. 14) because $P2_1/c$ is in a lower-symmetry subgroup of $Pnma$ and is often observed in double-perovskite materials. As shown in Fig. 1(a), the analysis is successful, indicating that the $Pnma$ model better describes the crystal structure of GSCO. The refined lattice parameters are $a = 5.41289(2)$ Å, $b = 7.63652(2)$ Å, and $c = 5.39966(2)$ Å. The atomic coordinates and isotropic thermal displacement parameters are shown in Table S1 in the Supplemental Material [60]. The inset of Fig. 1(a) shows a structural image of GSCO.

Considering the observed refined tendencies, when we refined the occupation factors for oxygen, the values were slightly $> 1$; the oxygen site is likely occupied fully. Thus, it was reasonable to fix the value to be 1 in the final step. Although the observed pattern was refined to a certain extent using the $P2_1/c$ model, the analysis was unsatisfactory. Detailed inspection, particularly temperature dependence, the standard errors for $\beta$ angle, and volume increased significantly with temperature. This indicated that GSCO did not crystallize in a monoclinic double-perovskite-based structure with a rock salt-type order.

Meanwhile, GCCO is analyzed well using the orthorhombic $Pnma$ model, which is common in most $RCrO_3$ materials. Notably, refining the pattern of GCCO using the monoclinic model ($P2_1/c$) failed. Because the end members $GdCrO_3$ [6] and $CaCrO_3$ [61] crystallize in the orthorhombic structure ($Pbnm$), GCCO may be regarded as a solid solution. In addition, several small peaks in the synchrotron XRD pattern indicate the presence of 2.5 wt. % orthorhombic $CaCr_2O_4$ [62]. Rietveld analysis refines the lattice parameters of GCCO and the overall scale factor simultaneously, but the structural parameters of the minor phase remain constant. The final analyzed synchrotron XRD pattern of GCCO is shown in Fig. 1(b), and detailed crystallographic data is shown in Table S2 in the Supplemental Material [60]. The refined lattice parameters are $a = 5.42543(1)$ Å, $b = 7.54252(1)$ Å, and $c = 5.31059(1)$ Å. For comparison, the inset of Fig. 1(b) shows a structural image of GCCO. The overall structure is similar for GSCO and GCCO at this image scale, but the structure has different degrees of local lattice distortion. For example, the Cr–O lengths of the $CrO_6$ octahedron differ by 0.25% in GSCO and 1.7% in GCCO.

Furthermore, synchrotron XRD patterns were collected at various temperatures from 120 to 750 K to investigate the temperature dependences of the structural properties of GSCO and GCCO. However, neither a change in symmetry nor any additional features were observed. The changes in the lattice parameters of GSCO and GCCO with temperature are shown in Figs. S1(a)–(b) and S1(c)–(d) in the Supplemental Material [60], respectively. All GSCO lattice parameters increase with increasing temperature, exhibiting the expected thermal behavior. The lattice parameters $a$ and $c$ almost converge at $\sim 750$ K (Fig. S1(a) in the Supplemental Material [60]), indicating that GSCO may approach a structural transition or thermal decomposition. In contrast, the GCCO lattice parameter $a$ decreases with increasing temperature (Fig. S1(c) in the Supplemental Material [60]), although the cause remains unknown. This issue should be investigated in future research.

### B. Magnetization

The temperature-dependent dc-$\chi$ of GSCO under an applied field of 0.1 kOe, as shown in Fig. 2(a), displays a clear anomaly in the FC curve at $\sim 98$ K [first derivative spectrum in the inset of Fig. 2(a)], revealing the onset of magnetic order. Below this temperature, the FC curve exhibits a small hump that intersects the zero line at $T_{comp} = 48$ K. With further cooling, $\chi$ decreases until the technical limit (2 K), which is commonly known as magnetization reversal. Conversely, the ZFC curve shows a very weak response at 98 K. Notably,
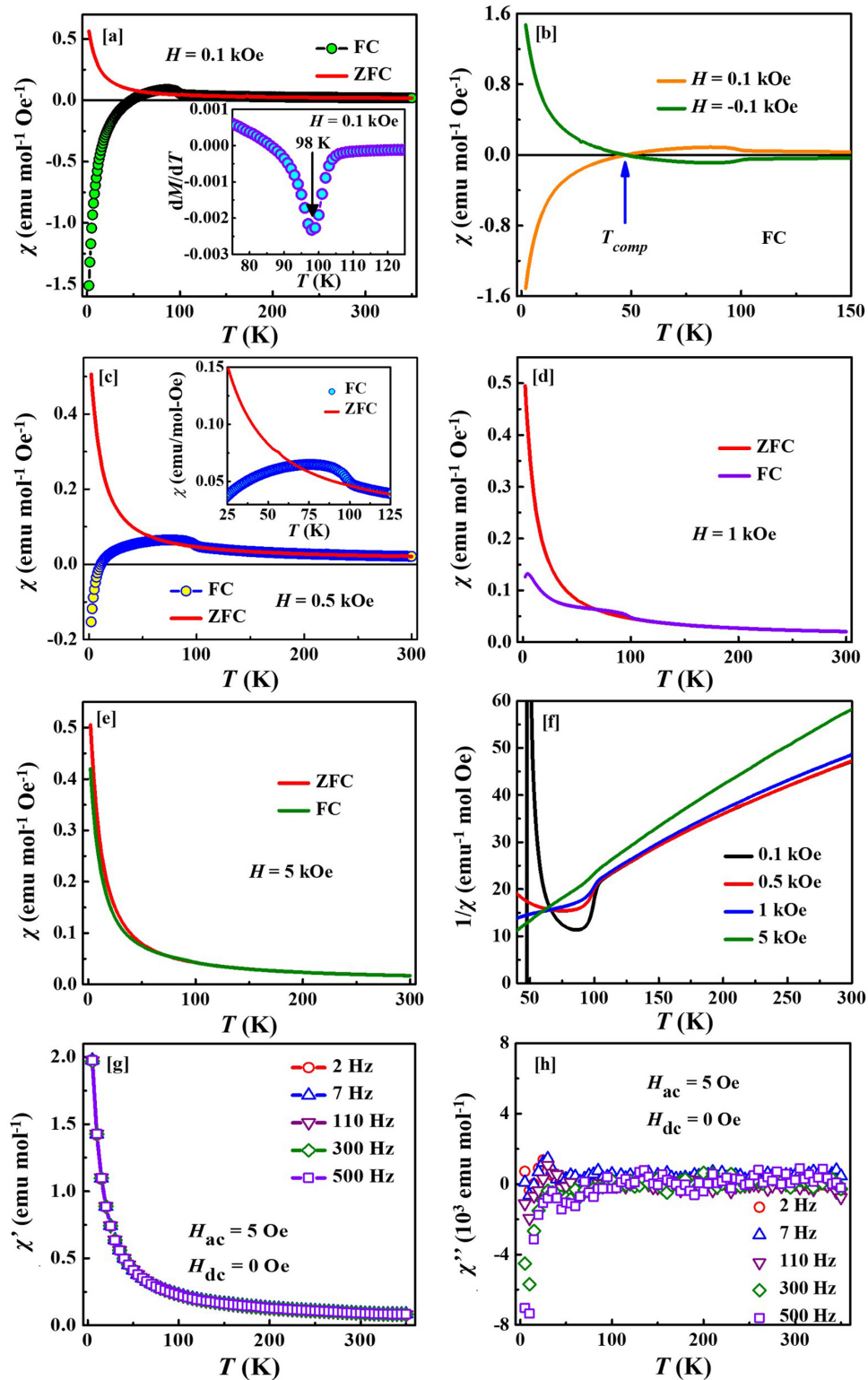
FIG. 2. (a) Zero-field-cooled (ZFC)- and field-cooled (FC)-$\chi(T)$ curves of GSCO measured in a magnetic field of $H = 0.1$ kOe. The inset shows the derivative curve of the FC curve. (b) FC-$\chi(T)$ curves of GSCO measured at $H = 0.1$ and $-0.1$ kOe. (c)–(e) ZFC- and FC-$\chi(T)$ curves measured at $H = 0.5$, 1, or 5 kOe, respectively. The inset of (c) displays an enlarged view of the ZFC- and FC-$\chi(T)$ curves at $H = 0.5$ kOe. (f) Inverse $\chi$ ($1/\chi$) as a function of temperature and applied field. (g) In-phase ($\chi'$) and (h) out-of-phase ($\chi''$) parts of ac-$\chi(T)$ of GSCO measured in an ac magnetic field of 5 Oe at various frequencies.

the FC and post-FC (when heated) curves follow the same trend, unlike those observed for GdCrO$_3$. Furthermore, GSCO exhibits no features related to the spin reorientation that occurs in GdCrO$_3$ [2,5].

As suggested by the GSCO structural analysis, Cr ions with different valences are likely connected by AFM exchange interactions and may induce long-range magnetic order at 98 K. Early studies report a similar magnetic behavior, i.e., by the canted FiM order of the double perovskite La$_2$Ni$_{1.19}$Os$_{0.81}$O$_6$ [63]. Thus, the developed magnetic order of GSCO is likely a canted FiM order, with a transition temperature $T_{FiM} = 98$ K. Moreover, the negative internal field on the Gd$^{3+}$ moments produced by the weak FM component of canted Cr$^{3+}$/Cr$^{4+}$ moments are responsible for the observed compensated magnetization and the magnetization reversal phenomenon below $T_{comp}$. The net moment from the two canted Cr$^{3+}$/Cr$^{4+}$ moments and the Gd$^{3+}$ moments have antiparallel coupling, thus exhibiting FiM ground state in GSCO. Nevertheless, in some ordered double perovskites ($R_2$BB$'$O$_6$, monoclinic structure with space group $P2_1/n$), the neutron powder diffraction studies confirmed that the FiM ground state is only identified by the coupling between rare-earth moments and FM component of B/B$'$ sublattices and not from the ordered B/B$'$ sublattice magnetization [64–66]. More importantly, the compensated magnetization and/or magnetization reversal phenomenon gives an exceptional indication about the FiM ground state in these kinds of materials, as well as in GSCO.

Under the ZFC condition, when a magnetic field is applied at the lowest temperature, the easy axes of the randomly oriented Gd moments are aligned along the magnetic field direction, and GSCO displays a positive $\chi$. When heated from 2 K, the Gd moments are thermally disturbed and $\chi$ decreases. As the magnetizations of the sublattices (Gd and Cr) are unequal, there is no compensation phenomenon.

The FC-$\chi$ curve at $H = -0.1$ kOe was also recorded to analyze whether the stray magnetic field plays a role in the observed magnetization reversal. The FC-$\chi$ curves measured at $H = 0.1$ and $-0.1$ kOe are plotted in Fig. 2(b). While measuring the FC-$\chi$ curve in the negative field, $\chi$ remains negative at $> T_{comp}$ and becomes positive at $< T_{comp}$, resembling the inverse behavior of that under the positive field. Because the curves exhibit mirror symmetry in terms of sign reversal, the stray magnetic field exerts little effect on the magnetization reversal.

Figures 2(c)–2(e) show the ZFC- and FC-$\chi$ curves measured in different fields ($H = 0.5$, 1, or 5 kOe). The magnetization reversal observed at $H = 0.1$ kOe gradually disappears as $H$ increases, and at $H \geqslant 1$ kOe, the magnetization reversal is challenging to observe. Notably, $T_{comp}$ decreases with increasing $H$ ($T_{comp} = 11$ K at $H = 0.5$ kOe), indicating the presence of a weaker negative internal field on the Gd moments (produced by weak FM components of the canted Cr moments in opposition to $H$).

The inverse susceptibility plots ($1/\chi$ vs $T$) shown in Fig. 2(f) reveal two main features: (i) a sharp decrease in $1/\chi$ at the onset temperature of the long-range magnetic order, which is reminiscent of the canted FiM order. (ii) True paramagnetic behavior is observed at temperatures of $\gg T_{FiM}(>\sim 200$ K), suggesting a short-range magnetic correlation between $T_{FiM}$ and $\sim 200$ K.

The sharp decrease in the $1/\chi$ curve softens with an increasing field, possibly due to the formation of short-range FM clusters. To confirm this, we analyzed the $1/\chi$ vs $T$ curves at 105 K $< T <$ 200 K using the power law expression of the Griffith singularity effect.

$$\frac{1}{\chi(T)} = A\left(T - T_C^R\right)^{1-\lambda},$$

where $A$ is a constant, $T_C^R$ is the critical temperature below which $\chi$ diverges, and $\lambda$ is an exponent [32,67]. Here, $1/\chi$ does not follow the power law expression well, signifying that the possible magnetic cluster behavior is non-Griffith-like. Similar non-Griffith-like behavior is observed in the half-doped cobaltite La$_{0.5}$Sr$_{0.5}$CoO$_3$, wherein AFM clusters are formed in the paramagnetic matrix [68].

Because we observe increasing magnetization of the pure paramagnetic phase by extrapolating the high-temperature Curie-Weiss (CW) line, short-range FM clusters, not AFM clusters, cause the observed non-Griffith-like behavior. Furthermore, $T_C^R$ is much lower than $T_{FiM}$, which is inconsistent with the anticipated behavior of a Griffiths phase (i.e., $T_C^R > T_{FiM}$). However, the short-range FM clusters are assumed to originate from the Cr$^{3+}$–O–Cr$^{4+}$ exchange interactions.

The ac-$\chi(= \chi' + i \chi'')$ of GSCO was measured in an ac magnetic field of 5 Oe at frequencies in the range 2–500 Hz. The in-phase ($\chi'$) and out-of-phase ($\chi''$) parts of the zero-field ac-$\chi$ as functions of $T$ are shown in Figs. 2(g) and 2(h), respectively. No sharp peak is observed at $T_{FiM}$, which is consistent with the weak responses of the dc ZFC-$\chi$ curves. No additional anomalies or magnetically glassy features are detected. Note that, if a cluster glasslike state is present in the material, a frequency range of up to 500 Hz is usually sufficient to detect it through ac-$\chi$ measurements [69–72].

In contrast, GCCO exhibits a completely different magnetic behavior. Figures 3(a)–3(c) show the dc ZFC- and FC-$\chi$ curves measured under various magnetic fields ($H = 0.05$, 0.1, or 0.5 kOe). The ZFC- and FC-$\chi$ curves are identical, increasing continuously as the temperature decreases. No onset of magnetic order is observed, as shown in the inset of Fig. 3(b). However, there is a clear difference between the ZFC and FC curves at $< 100$ K, as indicated by the arrows shown in Fig. 3(d). The divergence is much more pronounced in the first derivative, as shown in the inset of Fig. 3(d). The random substitution of Ca with Gd may lead to competition between the Cr$^{3+}$–O–Cr$^{3+}$ AFM superexchange and the Cr$^{3+}$–O–Cr$^{4+}$ FM double-exchange interactions, causing a magnetically disordered state. However, the divergence between the ZFC and FC curves may indicate that AFM interactions are slightly dominant. Thus, we specified the point of divergence as $T_N$ of GCCO. Since the local lattice distortion of GCCO is different from that of GSCO, its impact on the magnetic exchange interactions differs reasonably. Thus, the possible magnetic ground states of GSCO and GCCO are different owing to the strong dependence on the local structural properties. Notably, $\beta$-CaCr$_2$O$_4$ undergoes a magnetic transition characterized by the propagation vector
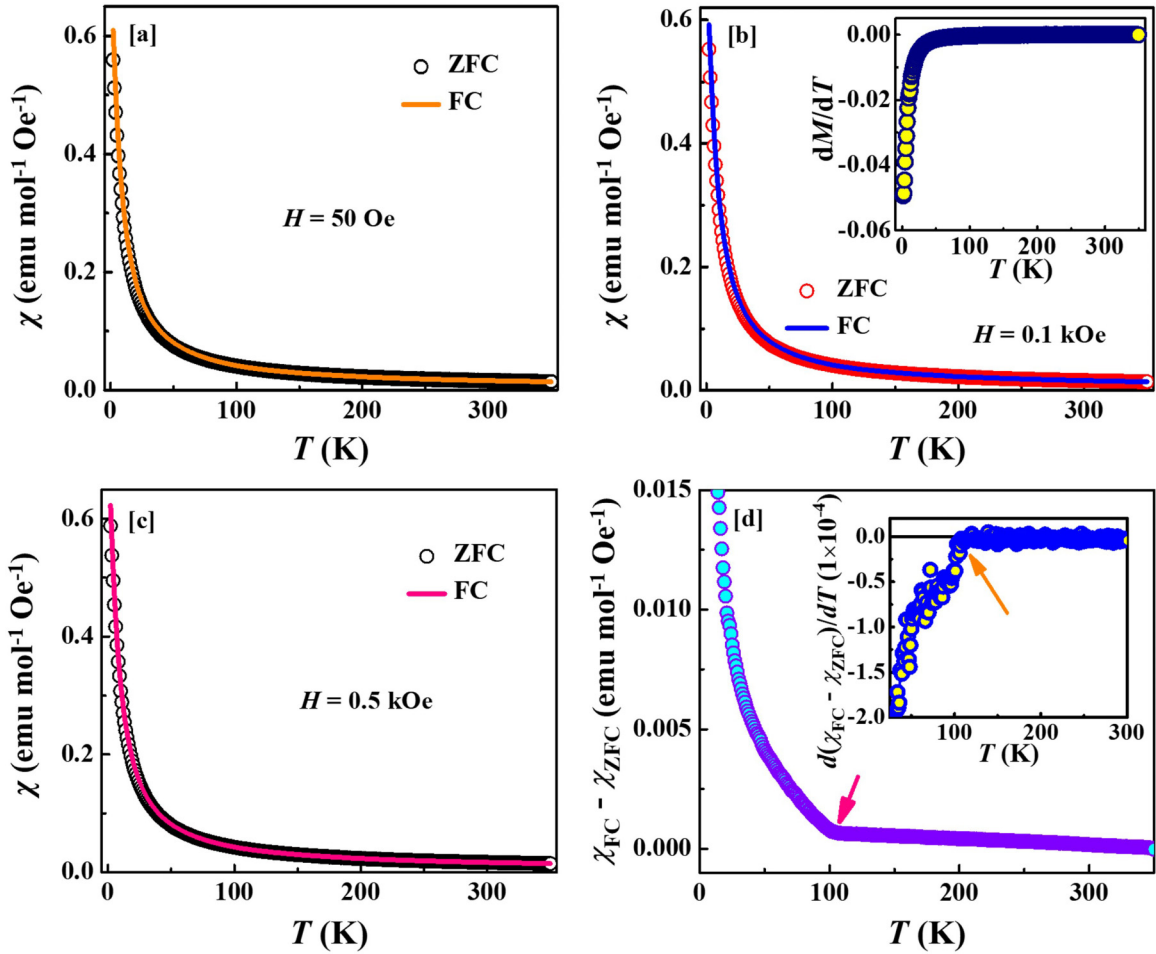
FIG. 3. (a)–(c) Zero-field-cooled (ZFC)- and field-cooled (FC)-$\chi(T)$ curves of GCCO measured at $H = 50$ Oe or 0.1 or 0.5 kOe, respectively. The inset of (b) shows the derivative curve at $H = 0.1$ kOe. (d) Difference between the ZFC- and FC-$\chi(T)$ curves at $H = 0.1$ kOe. Inset of (d) shows the derivative curve of $(\chi_{FC} - \chi_{ZFC})$.

$\mathbf{k} = (0, 0, \sim 0.477)$ at $T_N = 21$ K [62]. Although a small amount of $\beta$-CaCr$_2$O$_4$ (2.5 wt. %) is detected in GCCO, no corresponding feature is observed in the $\chi$ vs $T$ or $dM_{FC}/dT$ vs $T$ plots.

The thermal remanent magnetizations ($M_{TRM}$) of both materials were measured to further elucidate the onsets of the long-range magnetic order and short-range magnetic correlation. During measurement, the magnetic field was set to zero at 2 K immediately after cooling the sample from the paramagnetic state (350 K) in the presence of $H(= 0.5$ kOe), and the sample was then heated to measure the magnetization. Similar protocols are often used to study the spin dynamics of glassy magnetic materials. In addition, $M_{TRM}$ exhibits clear anomalies at the onset of the magnetic order [73,74]. Here, $M_{TRM}$ of GSCO and GCCO as functions of $T$ are shown in Figs. 4(a) and 4(b), respectively. The magnetization reversal of GSCO is again confirmed by the $M_{TRM}$ measurement. However, the thermal variation of $M_{TRM}$ differs slightly from that observed in the dc FC-$\chi$ measurement. In addition to the sharp increase in magnetization at the onset of long-range magnetic order at $T_{FiM}$, a clear anomaly is detected at $\sim 150$ K for GSCO [inset of Fig. 4(a)]. This indicates that a significant contribution from the short-range magnetic correlation begins at 150 K, which is $\gg T_{FiM}$. Conversely, GCCO exhibits an

increase in magnetization at $\sim 100$ K [Fig. 4(b)], which highlights the presence of the magnetic anomaly.

Figures 5(a) and 5(b) show the temperature-dependent $1/\chi$ values of GSCO ($H = 5$ kOe) and GCCO ($H = 0.1$ kOe), respectively. A moderately high magnetic field was used for GSCO to avoid other dilute magnetic interactions. The solid straight lines (red) shown in both plots are guidelines to aid in identifying deviations from CW behavior. The $1/\chi$ curves of GSCO and GCCO deviate from CW behavior at $< \sim 160$ and $< \sim 105$ K, respectively.

To obtain the CW parameters, we fitted the high-temperature $1/\chi$ curves to the CW equation $1/\chi = (T - \Theta)/C$, where $C = N_A \mu_{eff}^2 / 3k_B$ is the Curie constant, $N_A$ is Avogadro's number, $\mu_{eff}$ is the effective magnetic moment, $k_B$ is the Boltzmann constant, and $\Theta$ is the Weiss temperature. The fitted curves of GSCO and GCCO are displayed in the insets of Figs. 5(a) and 5(b), respectively, and the respective $\mu_{eff}$ values of GSCO and GCCO are 7.04 and 6.75 $\mu_B/$f.u. Because half of the Cr$^{3+}$ ions transform to Cr$^{4+}$ ions upon half-doping of Sr$^{2+}$ (Ca$^{2+}$) at the Gd site of GdCrO$_3$, the theoretical moments should be $\mu_{eff} = 6.53$ $\mu_B/$f.u., based on the equation:

$$\mu_{eff} = \sqrt{0.5\mu_{Gd}^2 + 0.5\mu_{Cr^{3+}}^2 + 0.5\mu_{Cr^{4+}}^2},$$
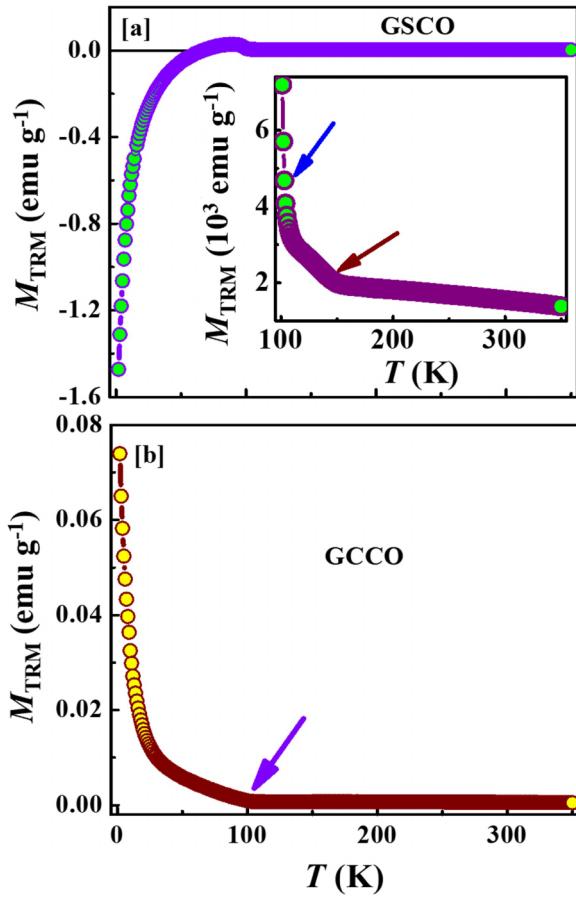
FIG. 4. Thermal remanent magnetizations ($M_{TRM}$) of (a) GSCO and (b) GCCO, which indicate the onset of magnetic ordering (arrows). The inset shows an enlarged view.
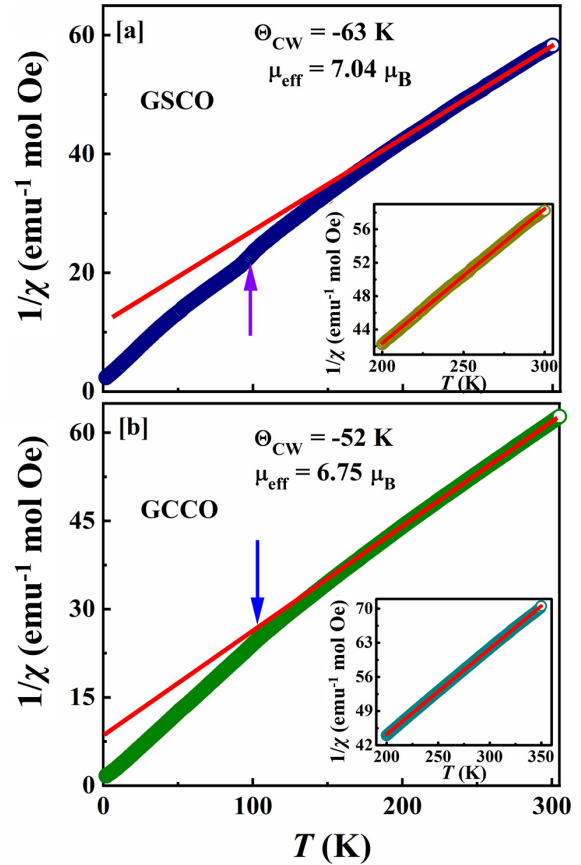


FIG. 5. Inverse magnetic susceptibilities ($1/\chi$) of (a) GSCO (at $H = 5$ kOe) and (b) GCCO (at $H = 0.1$ kOe) as functions of temperature. The solid red lines are guidelines for linear behavior, and the insets show the Curie-Weiss fittings of the high-temperature regions.

where $\mu_{Gd} = 7.90$ $\mu_B$, $\mu_{Cr3+} = 3.87$ $\mu_B$ (spin-only due to the quenched $3d$ orbital), and $\mu_{Cr4+} = 2.82$ $\mu_B$ (spin-only). This value is close to the experimentally observed values of GCCO and GSCO. In addition, the $\Theta$ values of GSCO and GCCO are $-63$ and $-52$ K, respectively, with the negative values indicating that AFM interactions are dominant in both materials.

To further elucidate the contrasting magnetic behaviors of these two materials, we recorded isothermal field-dependent magnetization ($M$ vs $H$) curves under ZFC conditions. Before the measurement of each $M$-$H$ curve, the material was cooled from well above the onset temperature of magnetic order to the targeted temperature under a zero magnetic field. Figure 6(a) shows the $M$-$H$ curves of GSCO at temperatures of 2, 10, 40, 60, and 85 K (all less than $T_{FiM}$). At $T = 40$, 60, or 85 K, linear changes in $M$ vs $H$ are observed in the high-field regions, but weak hystereses are observed in the low-field regions. Much wider hysteresis loops are observed at $T = 2$ or 10 K, indicating the presence of FM and AFM correlations below $T_{FiM}$.

Regarding the hysteresis loops, we plotted the values of the coercive field ($H_C$) based on the $M$-$H$ curves at different temperatures in Fig. 6(b). The decrease in $H_C$ at $< 85$ K may be related to the opposite orientation of the Gd sublattice owing to the negative internal field (i.e., the compensation

phenomenon) with respect to the applied field. An enlarged view of the isotherm at $T = 2$ K is shown in the inset of Fig. 6(b), which indicates that the $M$-$H$ loop closes within the range $\pm 20$ kOe.

Figure 6(c) shows the $M$-$H$ isotherms of GCCO at $T = 2$, 10, 40, 60, and 85 K. Here, $H_C$ is 40 Oe at 2 K, which is likely related to the AFM spin correlation. Moreover, even at 70 kOe, the $M$-$H$ curves are unsaturated, which is typical for materials with AFM-exchange interactions. Nevertheless, the significant S-shapes of the $M$-$H$ loops of GSCO and GCCO at $T = 2$ or 10 K may be due to the contributions from the much larger Gd$^{3+}$ moments.

To compare the magnetic properties of these two materials, we plotted the isothermal $M$-$H$ curves measured at $T = 2$ K, as shown in Fig. 6(d), with the inset showing an enlarged view. Notably, there is a small difference in the saturation magnetizations of these compounds at 70 kOe (3.05 and 3.17 $\mu_B$/f.u. for GSCO and GCCO, respectively), possibly due to the impurities in GCCO. Notably, the $H_C$ of GSCO ($= 1089$ Oe) is 27-fold larger than that of GCCO, which demonstrates its different magnetic nature. Generally, materials with canted FiM structures exhibit higher $H_C$ values than those of regular AFM materials. Current observations are in line with the general view.
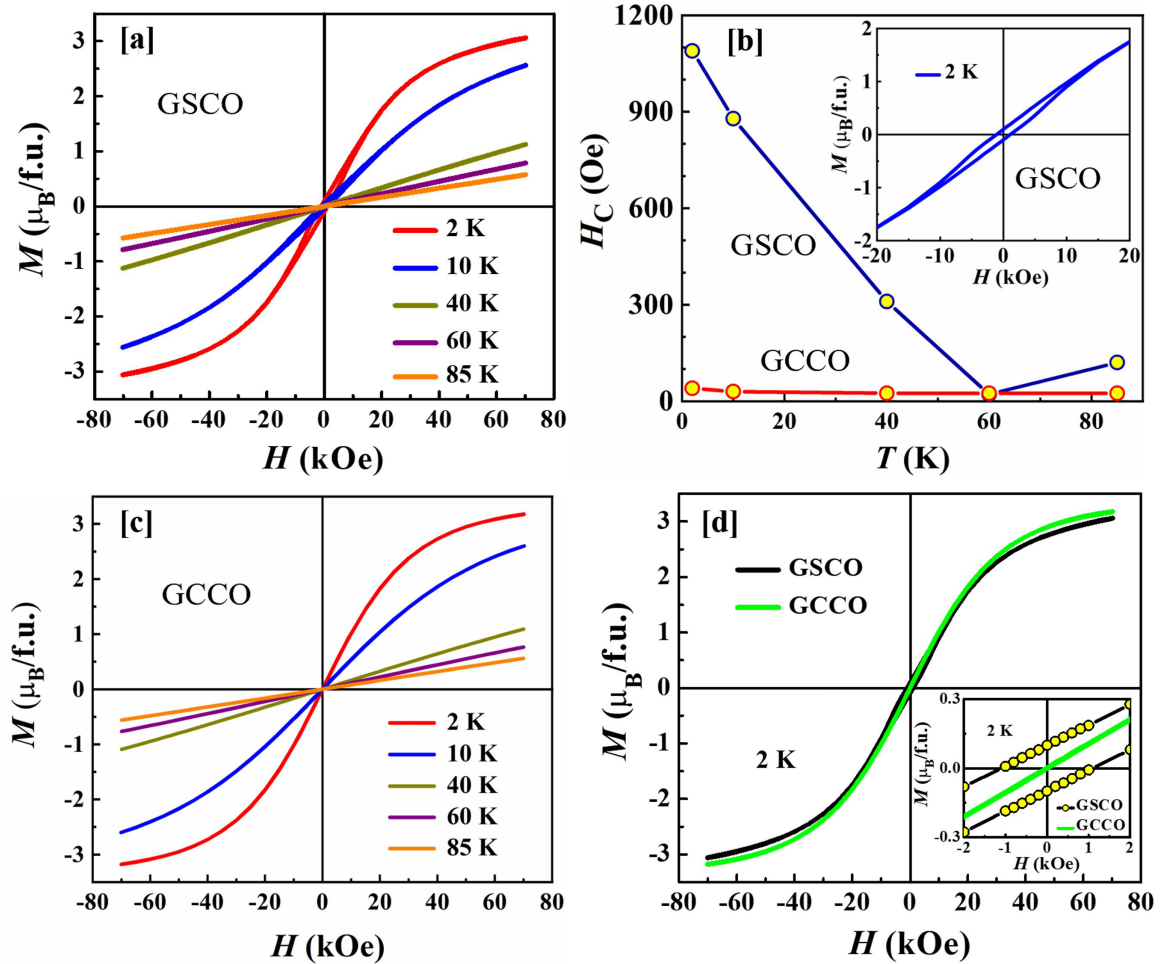
FIG. 6. (a) Isothermal magnetization ($M$) of GSCO as a function of magnetic field ($H$) measured under the zero-field-cooled (ZFC) condition at several temperatures ($T = 2$, 10, 40, 60, and 85 K). (b) Thermal variation of the coercive field ($H_C$), and the inset shows a magnified view of the ZFC $M$-$H$ loop at $T = 2$ K. (c) ZFC $M$-$H$ loops of GCCO measured at temperatures of 2, 10, 40, 60, and 85 K. (d) Comparison of the ZFC $M$-$H$ loops of GSCO and GCCO at 2 K. The inset shows an enlarged view.

In general, a heterogeneous material with two different magnetic states, such as FM and AFM states [75,76], an FM state and a spin glass [51,52], and FM and FiM states [77], sometimes results in the EB effect. This phenomenon, which is related to the shift of the $M$-$H$ loop along the magnetic field axis, has considerable applications in spintronic devices. Recently, the EB effect was also observed in a magnetically homogeneous material, i.e., FiM [14]. Because non-Griffith-like FM clusters and canted FiM states coexist in GSCO, we investigated the EB effects by measuring the FC $M$-$H$ loop at several temperatures. If the cooling field ($H_{cool}$) is positive, the FC $M$-$H$ loop shifts toward the negative field axis, which is widely recognized as the conventional EB effect. The EB field ($H_{EB}$) is a measure of EB anisotropy and defined as $H_{EB} = (H_1 + H_2)/2$, where $H_1$ and $H_2$ are the first (negative) and second (positive) coercive fields at the first and second magnetization reversals, respectively [51]. Notably, $H_{EB}$ should be negative in the conventional EB effect [76].

Figure 7(a) shows the FC $M$-$H$ loops of GSCO at $H_{cool} = 20$ kOe at various temperatures ($T = 2$, 10, 15, or 20 K) below $T_{FiM}$. Notably, the FC loops were measured within a maximum field ($H_{max}$) of ±20 kOe. Contrary to the symmetric

nature of a regular $M$-$H$ loop at the origin (absence of EB), the FC loop shifts slightly along the field direction from the origin, suggesting that EB anisotropy is induced upon field cooling. The FC loops at $T = 2$ K measured in different directions of $H_{cool} = 20$ and $-20$ kOe are shown in Fig. 7(b). The magnitude of the shift may be small, but the loop shifts in the opposite direction.

The enlarged views (within ±3 kOe) of the FC loops collected in the different directions of $H_{cool}$ at $T = 10$, 15, 20, 30, or 50 K are shown in Figs. 7(c)–7(g), respectively. Each loop shifts alternatively, i.e., the EB anisotropy undergoes sign reversal when $H_{cool}$ changes direction. Remarkably, the FC loop shifts toward the positive field axis when the material is cooled in the positive field, which contradicts the expectation of the conventional EB effect. This is known as the inverse EB (IEB) effect [78], and the FC loop exhibits the IEB effect at $T \leqslant 50$ K, whereas the conventional EB effect is observed at $T \geqslant 70$ K, e.g., an enlarged view of the FC loop within ±1 kOe at $T = 90$ K [Fig. 7(h)] reveals the conventional EB effect.

Figure 8 shows the temperature dependences of $H_1$, $H_2$, $H_C$, and $H_{EB}$ measured at a positive $H_{cool}$. Here, $H_1$ and $H_2$ are
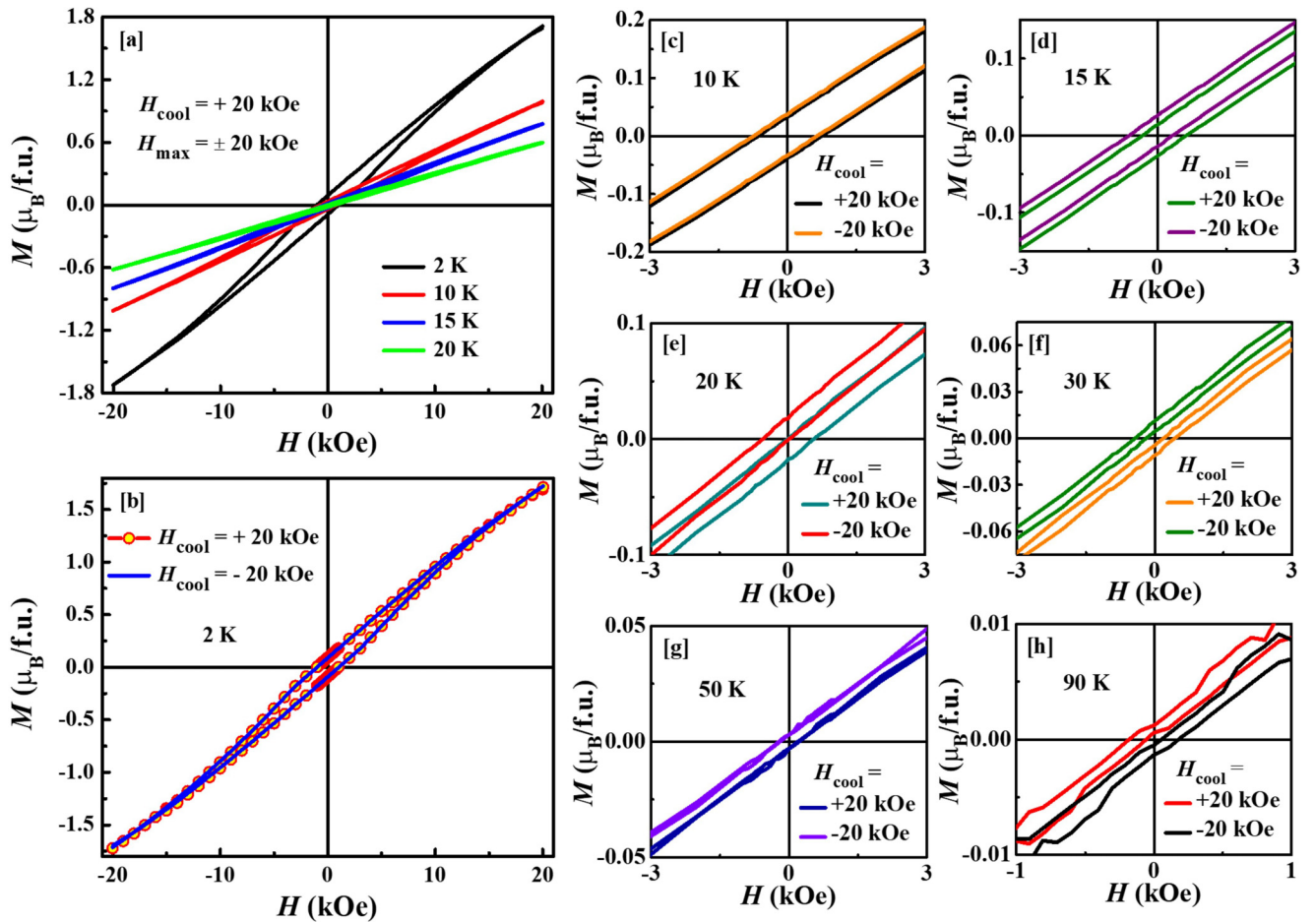
FIG. 7. (a) $M$-$H$ loops of GSCO measured at $H_{cool} = 20$ kOe. The maximum field is $\pm 20$ kOe, and the temperatures are $< T_{FiM}$. (b) Hysteresis loops measured at $T = 2$ K and $H_{cool} = 20$ or $-20$ kOe. (c)–(h) Magnified views of the field-cooled (FC) $M$-$H$ loops measured at $H_{cool} = \pm 20$ kOe and $T = 10$, 15, 20, 30, 50, or 90 K, respectively.

negative between 70 and 100 K but positive at $< 70$ K. Also, $H_2$ remains positive at $\geqslant 2$ K, and $H_1$ becomes negative again at $< 20$ K. Clearly, the $H_1$ and $H_2$ curves are not monotonous, and thus, a crossover from conventional EB to IEB effects (i.e., negative-to-positive sign inversion of $H_{EB}$) is observed in GSCO, which may be related to the observed magnetization reversal. Here, $H_{EB}$ approaches zero at $< 10$ K, confirming the absence of any EB effect. Apart from the small peak at $< T_{FiM}$, $H_C$ changes monotonically with temperature.

In general, in a strongly anisotropic system, where $M$ does not saturate at the highest $H$, the minor hysteresis loops hinder us from accurately estimating the EB parameters, which may ultimately lead to erroneous results. Therefore, to detect the true EB effect in such a system, considering an effectively saturated hysteresis loop is recommended [79]. When the loop is closed, $M$ is likely effectively saturated [51]. In this scenario, the FC and ZFC $M$-$H$ loops are fully closed at 2 K within $H_{max} = \pm 20$ kOe, as shown in Fig. 7(a) and the inset of Fig. 6(b), respectively. Therefore, the FM component may be saturated, and the minor hysteresis loops may exhibit little effect on the current analysis.

To study the effect of $H_{max}$ on the observed EB phenomenon, we investigated the FC loops at different $H_{max}$ values. FC loops measured at $T = 15$ K

(randomly selected) at a constant $H_{cool}(= 20$ kOe) and different $H_{max}(= \pm 20, \pm 25, \pm 30,$ or $\pm 70$ kOe) are shown in Fig. 9(a), and an enlarged view of the origin is shown in Fig. 9(b). The magnitude of $H_1$ increases with increasing $H_{max}$, and that of $H_2$ does not change, and thus, the EB effect is reduced by increasing $H_{max}$. Here, $H_C$ and $H_{EB}$ are plotted as functions of $H_{max}$ at $T = 15$ K in Fig. 9(c), with $H_C$ increasing rapidly up to $H_{max} = 35$ kOe, beyond which it increases only slightly. Conversely, $H_{EB}$ decreases sharply as $H_{max}$ increases from 20 to 30 kOe and is almost zero at $> 30$ kOe. In addition, the almost complete suppression of $H_{EB}$ at higher $H_{max}$ values may be associated with suppressed FM contributions from $Cr^{3+}/Cr^{4+}$ ions in the FiM structure. At $H_{max} \geqslant 30$ kOe, a large paramagnetic $Gd^{3+}$ moment dominates the entire magnetism, which inevitably reduces the exchange anisotropy between the FM clusters and FiM state.

Visualizing the origin of the EB effect, particularly the IEB effect, is rather complex, particularly in single-phase polycrystalline materials with invisible physical boundaries between the two different magnetic phases. Owing to the presence of FM clusters at high-temperatures, complex interfacial magnetic interactions between these clusters and the FiM state may induce EB anisotropy, causing the conventional EB effect in GSCO. Nevertheless, the presence of FM and
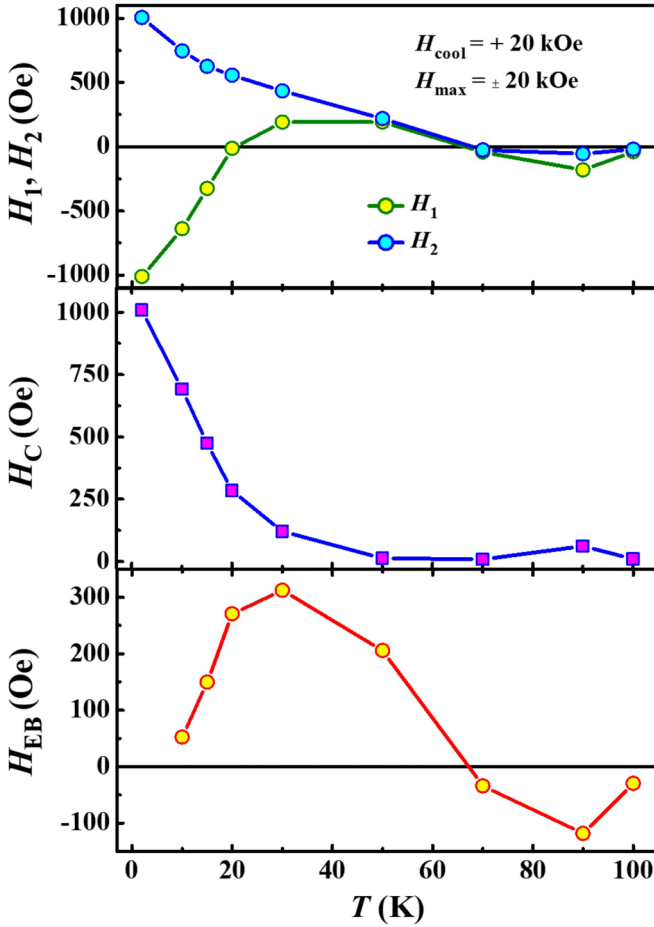
FIG. 8. Thermal profiles of $H_1$, $H_2$, $H_C$, and $H_{EB}$ obtained from the field-cooled (FC) $M$-$H$ loops of GSCO at $H_{cool} = 20$ kOe and $H_{max} = \pm 20$ kOe. Notably, the sign reversal of $H_{EB}$ from negative to positive occurs upon cooling.

AFM components specific to the FiM state may be the real cause of the observed conventional EB behavior.

To gain deeper insight into the IEB phenomenon, we analyzed possible mechanisms to elucidate its origin. In most earlier investigations [80–83], the phenomena of IEB manifest with increasing strength of $H_{cool}$, in addition to the conventional EB effect at lower $H_{cool}$ values. The sign reversal of $H_{EB}$ is successfully explained for a system wherein FM nanodroplets are embedded in a charge-ordered AFM host using the following equation:

$$-H_{EB} \propto J^2 A L(\mu, H_{cool}, T_f) + J H_{cool},$$

where $J$ is the surface exchange constant, $A$ is a constant (multiplication factor), and $L$ is the Langevin function of the magnetic moment $\mu$ of the FM nanodroplets $H_{cool}$ and freezing temperature $T_f$ of the interfacial spin [82]. Clearly, the competition between the surface exchange interaction and $H_{cool}$ may induce the sign reversal of $H_{EB}$. This equation shows that, for a lower $H_{cool}$, the first term dominates, and $H_{EB}$ becomes negative, as $J^2$ is always positive. For a higher $H_{cool}$, the second term may be significant, and in the case of AFM interfacial coupling, i.e., $J < 0$, sign reversal of $H_{EB}$ may be anticipated.
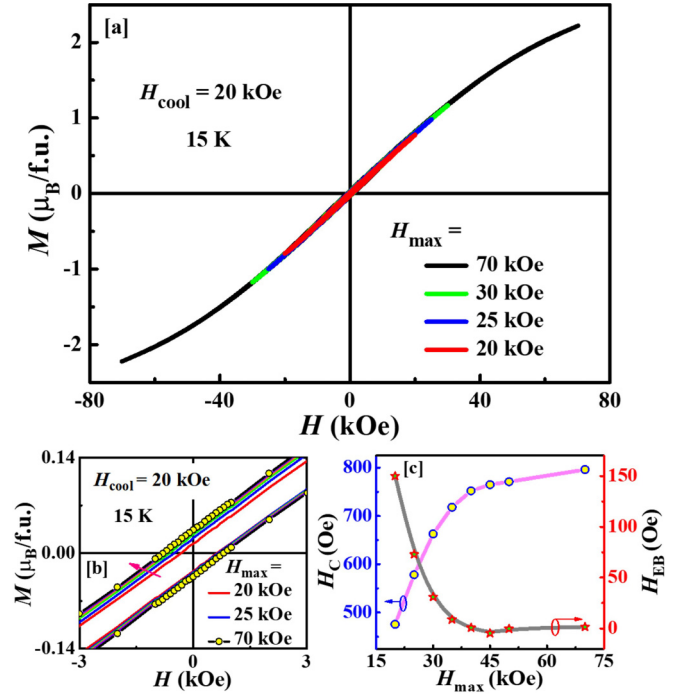


FIG. 9. (a) Field-cooled (FC) $M$-$H$ loops of GSCO measured at $T = 15$ K at $H_{cool} = 20$ kOe and $H_{max} = \pm 20$, $\pm 25$, $\pm 30$, or $\pm 70$ kOe. (b) Enlarged view of the loops. (c) $H_C$ and $H_{EB}$ as functions of $H_{max}$ ($H_{cool} = 20$ kOe) at $T = 15$ K.

In contrast, in this investigation, when $T$ is varied at a fixed $H_{cool}$ and the sign of $H_{cool}$ is changed at a fixed $T$, sign inversion of $H_{EB}$ is observed. Because the $H_{EB}$ equation does not contain $T$-dependent terms, the above prediction is unlikely. Another possibility in achieving the IEB effect is a magnetization reversal in the FiM state at $< T_{comp}$, which causes the IEB effect of LuFe$_{0.5}$Cr$_{0.5}$O$_3$ [78]. Because sign inversion of $H_{EB}$ is also detected at $< T_{comp}$ of the canted FiM GSCO, these two materials should share a basic physical mechanism. In addition, the various possible pathways of the DM interaction between two Cr ions (with different oxidation states) may lead to a reversal of the magnetic moment, thereby producing the IEB effect. Furthermore, the rough interface between the magnetic layers yields spatially varying mixed AFM and FM couplings, which may generate the IEB effect, even at a lower $H_{cool}$ [81]. In this paper, definitively identifying the origin of the IEB behavior of GSCO is challenging.

### C. Heat capacity

To better understand the magnetic properties, the specific heat capacities ($C_{total}$) of GSCO and GCCO were measured at $H = 0$ and 90 kOe. Figure 10(a) shows the zero-field ($H = 0$ kOe) $C_{total}(T)$ curve of GSCO, which exhibits no $\lambda$-like anomaly, which is a common feature of AFM transitions. Instead, a clear anomaly is observed close to $T_{FiM} = 98$ K [Fig. 2(a)]. To estimate the change in magnetic entropy ($S_m$) by subtracting the lattice contribution ($C_{lattice}$) from $C_{total}$, combinations of the Debye and Einstein [84] or the two Debye functions [85] were used to fit the high-temperature region of
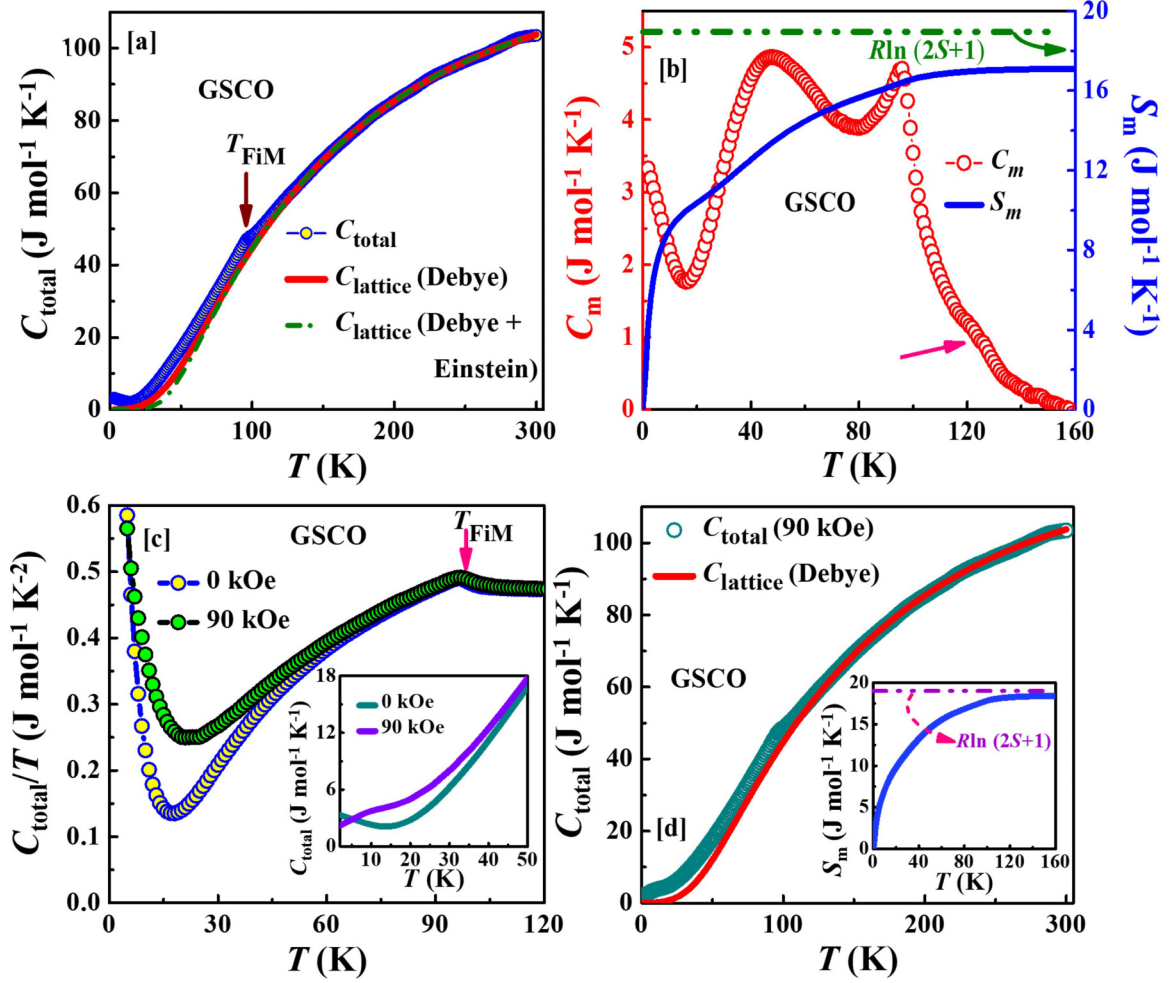
FIG. 10. (a) Temperature dependence of the specific heat capacity ($C_{\text{total}}$) of GSCO under a zero field. The solid and dashed curves show the lattice heat capacities ($C_{\text{lattice}}$) obtained by fitting to the high-temperature region with combinations of two Debye functions or Debye and Einstein functions, respectively. (b) Temperature dependences of the magnetic heat capacity ($C_m$), which is obtained by subtracting $C_{\text{lattice}}$ from $C_{\text{total}}$, and the magnetic entropy ($S_m$). The dash-dotted straight line represents the theoretical $S_m$. (c) $C_{\text{total}}/T$ vs $T$ plots of GSCO at $H = 0$ and 90 kOe. The inset shows the $C_{\text{total}}$ vs $T$ plots. (d) $C_{\text{total}}(T)$ of GSCO at $H = 90$ kOe. The solid red curve represents $C_{\text{lattice}}$ obtained by fitting to the high-temperature region with a combination of two Debye functions. The inset displays the $S_m$ vs $T$ curve.

$C_{\text{total}}(\gg T_{\text{FiM}})$. In the first case, the formula used is as follows:

$$C_{\text{total}}(T) = n_D \mathcal{D}(T, \Theta_D) + n_E \mathcal{E}(T, \Theta_E),$$

where $\mathcal{D}$ and $\mathcal{E}$ are the Debye and Einstein functions, respectively. Here, $\Theta_D$ and $\Theta_E$ are the respective Debye and Einstein temperatures, and the scale factors $n_D$ and $n_E$ correspond to the numbers of vibrational modes per formula unit in the Debye and Einstein models, respectively. In the latter case, the heat capacity is approximated by

$$C_{\text{total}}(T) = m_1 \mathcal{D}(T, \Theta_{D1}) + m_2 \mathcal{D}(T, \Theta_{D2}),$$

where $m_1$ and $m_2$ are the coefficients related to the vibrational modes per formula unit and $\Theta_{D1}$ and $\Theta_{D2}$ are the characteristic Debye temperatures. In both cases, proper fitting is observed with the parameters $n_D = 2.34$, $\Theta_D = 859$ K, $n_E = 2.73$, $\Theta_E = 273$ K, $m_1 = 2.09$, $m_2 = 2.99$, $\Theta_{D1} = 888$ K, and $\Theta_{D2} = 385$ K. The total number of vibrational modes in both cases is $\sim 5$ (i.e., $n_D + n_E \approx 5$ and $m_1 + m_2 \approx 5$), which validates the presence of five atoms per formula unit of GSCO.

Here, $C_{\text{lattice}}$ dominates $C_{\text{total}}$ at temperatures of $\gg T_{\text{FiM}}$, and thus, the fitted parameters enable the extrapolation of $C_{\text{lattice}}$ to the low-temperature limit, as shown by the solid and dotted lines [for $C_{\text{lattice}}$ (Debye) and $C_{\text{lattice}}$ (Debye + Einstein), respectively] displayed in Fig. 10(a). Because the observed $C_{\text{total}}$ and Debye (only) models are very similar, we adopted $C_{\text{lattice}}$ (Debye) as a reference to examine the lattice contribution for further analysis. Notably, there is no similar nonmagnetic material that may be used as a reference to properly estimate $C_{\text{lattice}}$ of GSCO.

The magnetic contribution to the heat capacity ($C_m$) is estimated by subtracting $C_{\text{lattice}}$ from $C_{\text{total}}$, i.e., $C_m(T) = C_{\text{total}}(T) - C_{\text{lattice}}(T)$. Figure 10(b) shows $C_m$ as a function of $T$, revealing a sharp peak close to $T_{\text{FiM}} = 98$ K. Additionally, the data show a broad peak at $\sim 45$ K, with another increase at $< 15$ K. The broad peak at $< T_{\text{FiM}}$ is unusual and is likely due to magnetization reversal, and the increase at $< 15$ K may be due to the short-range AFM ordering of the Gd moments. Similar increases in $C_{\text{total}}$ are also reported in single-crystal and polycrystalline Gd$_2$CoMnO$_6$ [86,87] and single-crystal

$Tb_2CoMnO_6$ [88]. In addition, an extended plateau of the peak at $\sim T_{FiM}$ is observed in the high-temperature region of $C_m$, which suggests the possible presence of short-range magnetic correlations at $> T_{FiM}$. Moreover, the $C_m(T)$ curve displays several remarkable features but is too complicated to understand clearly.

Finally, $S_m$ is estimated by integrating $C_m(T)/T$ over the studied temperature range [Fig. 10(b)]. Here, $S_m$ increases rapidly with increasing temperature at $\leqslant 10$ K, then gradually increases with increasing temperature, and plateaus at 17 J mol$^{-1}$ K$^{-1}$ at $> 130$ K. However, the saturation value of $S_m$ is slightly smaller than the expected Boltzmann entropy [$S_m = R\ln(2S+1) \approx 19$ J mol$^{-1}$ K$^{-1}$] based on the mean-field theory for localized $Cr^{3+}(S = \frac{3}{2})$, $Cr^{4+}$ ($S = 1$), and $Gd^{3+}(S = \frac{7}{2}, L = 0)$. The dashed line in Fig. 10(b) represents the Boltzmann entropy. Several factors may cause the slight discrepancy between the observed and expected $S_m$, one of which is the short-range AFM ordering of $Gd^{3+}$ moments. In addition, the inadequate estimation of $C_m$ at very low temperatures by extrapolating the high-temperature $C_{lattice}$ may be another cause of the discrepancy. Furthermore, increasing $C_{total}$ at the lowest temperature [2 K, inset in Fig. 10(c)] hinders the proper estimation of $C_m$.

The $C_{total}/T$ vs $T$ curves of GSCO at $H = 0$ or 90 kOe are plotted in Fig. 10(c). Even at $H = 90$ kOe, no noticeable suppression at $\sim T_{FiM}$ is observed. Instead, the valleylike features centered at $\sim 15$ K are moderately suppressed. As shown in the inset of Fig. 10(c), $C_{total}$ at $H = 90$ kOe does not increase as it does under the zero-field but decreases toward zero at $< 5$ K. Additionally, the short-range ordering of $Gd^{3+}$ moments are significantly disturbed by the application of the 90 kOe field (due to the increased $Gd^{3+}$ polarization). We attempted to estimate the saturation value of $S_m$ again by determining $C_{lattice}$ by fitting the high-temperature region of the $C_{total}$ (90 kOe) curve using the combination of the two Debye functions and extrapolating to $T = 0$ K [Fig. 10(d)]. Remarkably, the temperature dependence of $S_m$ [inset in Fig. 10(d)] shows that $S_m$ generally saturates at a value much closer to the Boltzmann entropy than that at $H = 0$ kOe. Thus, the discrepancy between the observed ($H = 0$ kOe) and expected $S_m$ is likely caused by short-range AFM ordering of $Gd^{3+}$ moments.

To facilitate further comparative studies, we performed a detailed analysis of $C_{total}$ of GCCO. Remarkably, the temperature dependences of the zero-field $C_{total}(T)$ of both materials are very similar [Figs. 10(a) and 11(a) show those of GSCO and GCCO, respectively], but a clear anomaly is observed at $\sim 100$ K in the $C_{total}(T)$ curve of GCCO. The observed anomalies and magnetization data indicate that GCCO undergoes AFM ordering at $\sim 100$ K. The solid red line shown in Fig. 11(a) represents the GCCO $C_{lattice}$ estimated by combining the two Debye functions. Anomalies are detected at $\sim 100$ K, but no sharp peaks are observed in the $C_m(T)$ plot close to this temperature (not shown). Instead, a broad peak and an upturn at $\sim 75$ and $< 15$ K are observed, respectively.

As shown in the inset of Fig. 11(a), when the temperature is $> 130$ K, $S_m$ saturates at 17.5 J mol$^{-1}$ K$^{-1}$, which is slightly smaller than the expected Boltzmann entropy. At $H = 90$ kOe, $C_{total}(T)$ displays no significant change in the
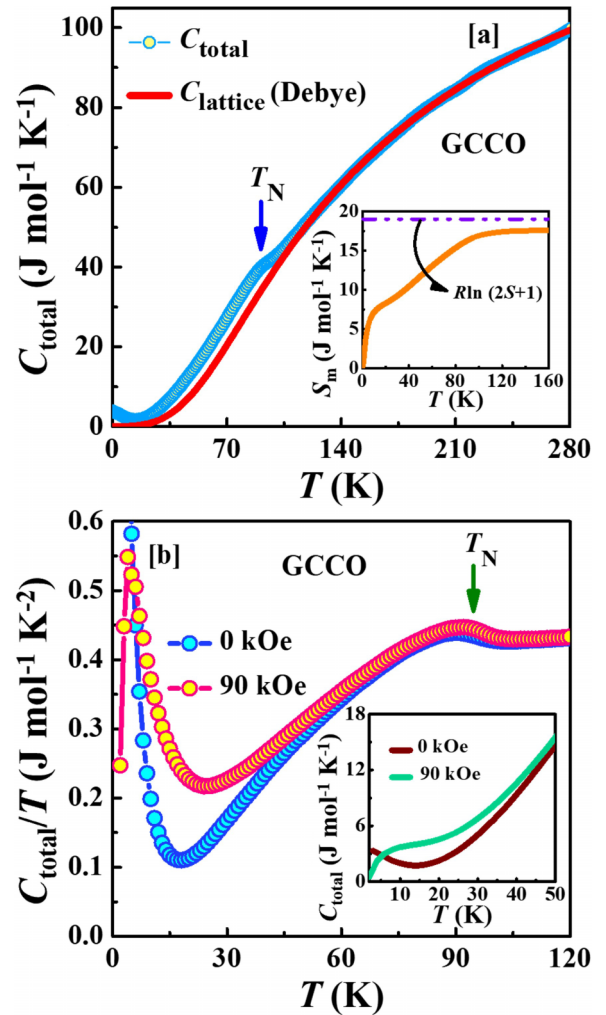


FIG. 11. (a) Specific heat capacity of GCCO as a function of temperature. The red solid curve shows a fitting to a combination of Debye functions, and the inset shows the thermal profile of $S_m$ of GCCO and the theoretical value. (b) $C/T$ vs $T$ plots of GCCO at $H = 0$ or 90 kOe. The inset shows the $C_{total}$ vs $T$ plots.

magnetic transition at 100 K [$C/T$ vs $T$ plot in Fig. 11(b)]. Conversely, valleylike features at 15 K, such as those observed for GSCO, are strongly influenced by the application of $H$. The inset in Fig. 11(b) shows an enlarged view of the $C_{total}(T)$ curves at $H = 0$ or 90 kOe, revealing that they intersect at $T = 5$ K.

### D. Resistivity

Figure 12(a) shows the temperature-dependent resistivities $\rho(T)$ of GSCO and GCCO. The increase in resistivity with decreasing temperature should yield semiconductorlike behavior. In this context, measuring $\rho(T)$ at temperatures of $< 70$ K was impossible because of the high resistance which was above the instrumental limit. At room temperature, $\rho$ of GSCO is almost 14-fold higher than that of GCCO ($\rho_{300 K} = 57.01$ and $4.19$ $\Omega$-cm for GSCO and GCCO, respectively). No metallic behavior is observed within the investigated temperature range, and these features contrast with the electrical
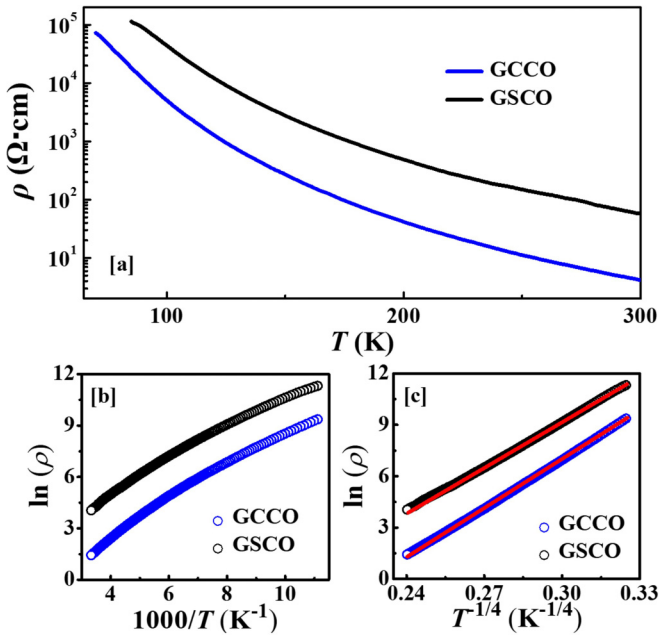
FIG. 12. (a) Temperature dependences of $\rho$ of GSCO and GCCO. (b) Alternative plot of the data. (c) Variable-range-hopping plot of the data. The red solid lines are guidelines.

behaviors of half-doped manganites and cobaltites [36,50]. The resistivity data were analyzed using the Arrhenius model, $\ln\rho$ vs $1000/T$, to investigate the possible conduction mechanisms, as shown in Fig. 12(b). Owing to the nonlinear behaviors of the curves, the $\rho(T)$ curves of both materials are not well modeled by the Arrhenius model. Instead, the linear behavior of the $\ln\rho$ vs $T^{-1/4}$ plot [Fig. 12(c)] shows that variable-range hopping better explains the observed electronic behaviors of GSCO and GCCO.

### E. Dielectric behavior

Several $R\mathrm{CrO_3}$ materials (excluding $R =$ Sc–Pr, Pm, Eu, Dy, Yb) should exhibit significant magnetoelectric coupling at temperatures of $< T_N$, and thus, they are potential multiferroic materials. Temperature-dependent relative permittivity ($\varepsilon_r$) measurements of GSCO and GCCO were performed at various frequencies to investigate possible magnetoelectric coupling. The thermal changes in $\varepsilon_r$ and its loss factor ($\tan\delta$) are shown in Figs. 13(a)–13(d). The $\varepsilon_r(T)$ curves of both materials display three main characteristics: (i) low-$T$ plateaus at $\varepsilon_r$ of $\sim 60$; (ii) sharply increasing $\varepsilon_r$ close to $T = 30$ K (at 100 Hz), which is strongly frequency-dependent; and (iii) significant anomalies at $T \approx 100$ K (magnetic transition temperatures of GSCO and GCCO). These are also strongly frequency dependent and shift toward a higher $T$ as the frequency increases [Figs. 13(a) and 13(b)].

In addition, the dielectric anomalies observed at $T_{\mathrm{FiM}}$ (for GSCO) and $T_N$ (for GCCO) confirm the presence of significant magnetoelectric coupling in both materials. The frequency dependence of the dielectric anomaly ($\sim T_{\mathrm{FiM}}$ and $\sim T_N$) is characteristic of a ferroelectric relaxorlike state, e.g., spontaneous electrical polarization associated with the anomaly is observed in $R\mathrm{CrO_3}$ [12] and the stepwise

increase in $\varepsilon_r$ at $\sim 30$ K may be associated with a large frequency-dependent Maxwell-Wagner relaxation [89]. This usually manifests itself as a depletion layer contribution at the interface between the sample and the electrodes or at some grain boundaries. Most importantly, it is not an inherent property of the material but an extrinsic issue. Conversely, the derivative spectra of $\varepsilon_r(T)$ exhibit two peaks at $T =\sim 100$ K ($T_{\mathrm{FiM}}$ and $T_N$), and the stepped increase in $\varepsilon_r$ at this temperature indicates the presence of magnetic coupling. For clarity, the derivative spectra of the data measured at 2.71 kHz are shown as examples [insets in Figs. 13(a) and 13(b)].

Strong dielectric losses are observed at this temperature, with stepwise increases in $\varepsilon_r$ observed [Figs. 13(c) and 13(d)]. The dielectric loss peaks depend on the frequency for both materials. No additional anomalies are observed in these spectra at the magnetic transition temperature, but the derivatives of the loss spectra reveal sharp increases at $\sim T_{\mathrm{FiM}}$ and $\sim T_N$ [as indicated by the arrows and insets in Figs. 13(c) and 13(d)]. Therefore, the dielectric loss spectra reveal the magnetoelectric coupling of both materials. In addition, the application of a magnetic field of 90 kOe results in no significant changes in the $\varepsilon_r(T)$ curves and dielectric loss spectra (not shown).

### IV. SUMMARY AND CONCLUSIONS

We successfully synthesized the half-doped perovskite-type chromites GSCO and GCCO. These polycrystalline materials were obtained via solid-state reactions at a high pressure and temperature (6 GPa and 1200 °C). Synchrotron XRD at room temperature revealed that GSCO and GCCO crystallized in orthorhombic structures (space group: *Pnma*) with different degrees of local lattice distortion.

We observed magnetization reversal in GSCO, but GCCO displayed a little anomaly. The magnetic ground state of GSCO is FiM, while it is AFM for GCCO. Therefore, the magnetic ground state of half-doped $\mathrm{GdCrO_3}$ could be tuned via substitution with various alkaline-earth ions. Moreover, the different magnetic ground states of GSCO and GCCO possibly originate from the different degrees of local lattice distortions, as evident from the structural analysis. In addition, thermal residual magnetization studies confirmed the presence of short-range magnetic correlations within GSCO at temperatures of $> T_{\mathrm{FiM}}$. This was further supported by the heat capacity measurements.

Remarkably, GSCO displayed a crossover from the conventional EB effect to the IEB effect upon cooling. Such a crossover could be caused by the reversal of the magnetic moment due to various competing DM interactions. In general, the key factors of producing DM interaction between two atomic spins are the structural inversion symmetry breaking and the strong spin-orbit coupling (SOC) with magnetic exchange energy. In most cases, the strong SOC is provided by the neighboring atoms in the structure. However, in this paper, since $L = 0$ (for $\mathrm{Gd^{3+}}$), the orbital contribution from the neighboring $\mathrm{Gd^{3+}}$ cannot be expected. Therefore, the crystal structure itself may stabilize spin canting by minimizing some free energy [71,90,91]. Moreover, the complex interfacial magnetic interactions between the high-temperature FM clusters and the FiM state is the plausible origin of the
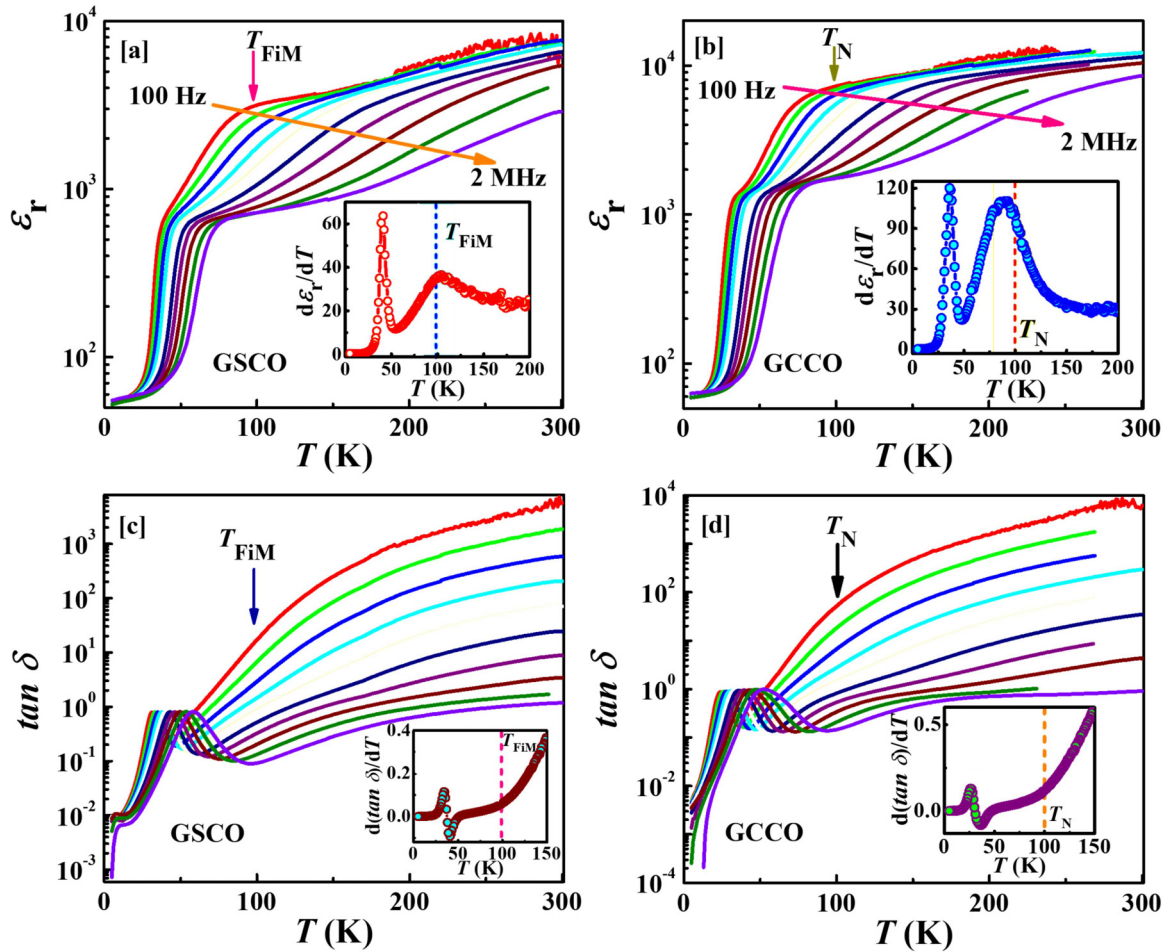
FIG. 13. (a)–(b) Temperature dependences of the dielectric constants ($\varepsilon_r$) of GSCO and GCCO, respectively, as recorded at several frequencies in the range 100 Hz–2 MHz ($f$ = 100 Hz, 300 Hz, 903 Hz, 2.71 kHz, 8.15 kHz, 24.51 kHz, 73.68 kHz, 221.43 kHz, 665.48 kHz, and 2 MHz). The insets show representative differential curves (at 2.71 kHz). The blue and red dashed lines in the insets indicate the temperature corresponding to the onset of magnetic order of each material. (c)–(d) Temperature-dependent dielectric losses (tan $\delta$) of GSCO and GCCO, respectively. The insets show representative differential curves (at 2.71 kHz).

conventional EB behavior in GSCO. Although several mechanisms including the competition between interfacial exchange coupling and $H_{cool}$, the reversal of magnetic moments below $T_{comp}$, and the spatially varying mixed AFM and FM couplings at the rough interface have been discussed to understand the origin of IEB, we can predict that the IEB effect in GSCO arises due to the magnetization reversal phenomenon. In addition, significant magnetoelectric coupling with ferroelectric relaxorlike states was identified at the onsets of magnetic order of both materials. The presence of the EB effect, particularly the IEB effect, and magnetoelectric coupling yields considerable prospects for application in magnetic memory and spintronic devices.

We interpreted the possible magnetic ground states of both materials as much as possible based on the experimental data, but the exact magnetic structures remain unclear because conducting neutron diffraction studies of highly

neutron-absorbing materials is technically challenging. Further combined studies, such as x-ray magnetic circular dichroism and density functional theory calculations, should contribute to a comprehensive understanding of the magnetic and electronic properties of these half-doped perovskite-type chromites.

[1] L. Holmes, M. Eibschtz, and L. G. Van Uitert, J. Appl. Phys. **41**, 1184 (1970).

[2] A. H. Cooke, D. M. Martin, and M. R. Wells, J. Phys. C: Solid State Phys. **7**, 3133 (1974).

[3] T. Morishita, K. Aoyagi, K. Tsushima, and T. Kigawa, Solid State Commun. **20**, 123 (1976).

[4] K. Toyokawa, S. Kurita, and K. Tsushima, Phys. Rev. B **19**, 274 (1979).

[5] K. Yoshii, J. Solid State Chem. **159**, 204 (2001).

[6] B. Rajeswaran, D. I. Khomskii, A. K. Zvezdin, C. N. R. Rao, and A. Sundaresan, Phys. Rev. B **86**, 214409 (2012).

[7] S. Lei, L. Liu, C. Wang, C. Wang, D. Guo, S. Zeng, B. Cheng, Y. Xiao, and L. Zhou, J. Mater. Chem. A **1**, 11982 (2013).

[8] K. R. S. Preethi Meher, A. Wahl, A. Maignan, C. Martin, and O. I. Lebedev, Phys. Rev. B **89**, 144401 (2014).

[9] A. McDannald, C. R. delaCruz, M. S. Seehra, and M. Jain, Phys. Rev. B **93**, 184430 (2016).

[10] B. Dalal, B. Sarkar, V. D. Ashok, and S. K. De, J. Phys.: Condens. Matter **28**, 426001 (2016).

[11] M. Taheri, F. S. Razavi, Z. Yamani, R. Flacau, P. G. Reuvekamp, A. Schulz, and R. K. Kremer, Phys. Rev. B **93**, 104414 (2016).

[12] A. Indra, K. Dey, A. Midya, P. Mandal, O. Gutowski, U. Rütt, S. Majumdar, and S. Giri, J. Phys.: Condens. Matter **28**, 166005 (2016).

[13] M. Tripathi, R. J. Choudhary, D. M. Phase, T. Chatterji, and H. E. Fischer, Phys. Rev. B **96**, 174421 (2017).

[14] B. Dalal, B. Sarkar, S. Rayaprol, M. Das, V. Siruguri, P. Mandal, and S. K. De, Phys. Rev. B **101**, 144418 (2020).

[15] I. Dzyaloshinsky, J. Phys. Chem. Solids **4**, 241 (1958).

[16] T. Moriya, Phys. Rev. **120**, 91 (1960).

[17] I. Fita, R. Puzniak, A. Wisniewski, and V. Markovich, Phys. Rev. B **100**, 144426 (2019).

[18] L. H. Yin, J. Yang, X. C. Kan, W. H. Song, J. M. Dai, and Y. P. Sun, J. Appl. Phys. **117**, 133901 (2015).

[19] Y. Zhu, P. Zhou, T. Li, J. Xia, J. Wu, Y. Fu, K. Sun, Q. Zhao, Z. Li, Z. Tang *et al.*, Phys. Rev. B **102**, 144425 (2020).

[20] J. van den Brink, G. Khaliullin, and D. I. Khomskii, Phys. Rev. Lett. **83**, 5118 (1999).

[21] F. Damay, C. Martin, A. Maignan, M. Hervieu, B. Raveau, Z. Jirak, G. André, and F. Bourée, Chem. Mater. **11**, 536 (1999).

[22] R. J. Goff and J. P. Attfield, Phys. Rev. B **70**, 140404(R) (2004).

[23] J. Padilla-Pantoja, J. Herrero-Martín, P. Gargiani, S. M. Valvidares, V. Cuartero, K. Kummer, O. Watson, N. B. Brookes, and J. L. García-Muñoz, Inorg. Chem. **53**, 8854 (2014).

[24] J. Padilla-Pantoja, J. Herrero-Martín, E. Pellegrin, P. Gargiani, S. M. Valvidares, A. Barla, and J. L. García-Muñoz, Phys. Rev. B **92**, 245136 (2015).

[25] E. O. Wollan and W. C. Koehler, Phys. Rev. **100**, 545 (1955).

[26] J. B. Goodenough, Phys. Rev. **100**, 564 (1955).

[27] Y. Tomioka, A. Asamitsu, Y. Moritomo, H. Kuwahara, and Y. Tokura, Phys. Rev. Lett. **74**, 5108 (1995).

[28] Y. Tokura, Rep. Prog. Phys. **69**, 797 (2006).

[29] E. Dagotto, New J. Phys. **7**, 67 (2005).

[30] E. Dagotto, Science **309**, 257 (2005).

[31] J. A. Souza, J. J. Neumeier, and Y. -K. Yu, Phys. Rev. B **78**, 014436 (2008).

[32] M. B. Salamon, P. Lin, and S. H. Chun, Phys. Rev. Lett. **88**, 197203 (2002).

[33] J. Fan, L. Pi, Y. He, L. Ling, J. Dai, and Y. Zhang, J. Appl. Phys. **101**, 123910 (2007).

[34] C. Autret, C. Martin, M. Hervieu, A. Maignan, B. Raveau, G. André, F. Bourée, and Z. Jirak, J. Magn. Magn. Mater. **270**, 194 (2004).

[35] K. Tobe, T. Kimura, and Y. Tokura, Phys. Rev. B **69**, 014407 (2004).

[36] H. Kawano, R. Kajimoto, H. Yoshizawa, H. Tomioka, H. Kuwahara, and Y. Tokura, Phys. Rev. Lett. **78**, 4253 (1997).

[37] V. K. Shukla and S. Mukhopadhyay, Phys. Rev. B **97**, 054421 (2018).

[38] C. R. Serrao, A. Sundaresan, and C. N. R. Rao, J. Phys.: Condens. Matter **19**, 496217 (2007).

[39] T. Zou, F. Wang, Y. Liu, L.-Q. Yan, and Y. Sun, Appl. Phys. Lett. **97**, 092501 (2010).

[40] S. Dash, A. Banerjee, and P. Chaddah, J. Appl. Phys. **113**, 17D912 (2013).

[41] S. M. Zhou, L. Shi, H. P. Yang, Y. Wang, L. F. He, and J. Y. Zhao, Appl. Phys. Lett. **93**, 182509 (2008).

[42] E. Dagotto, *Nanoscale Phase Separation and Colossal Magnetoresistance: The Physics of Manganites and Related Compounds* (Springer-Verlag, Berlin, Heidelberg, 2003).

[43] A. I. Kurbakov, V. A. Ryzhov, V. V. Runov, E. O. Bykov, I. I. Larionov, V. V. Deriglazov, C. Martin, and A. Maignan, Phys. Rev. B **100**, 184424 (2019).

[44] H. Zhou, Q. Feng, Y. Hou, M. Nakamura, Y. Tokura M. Kawasaki, Z. Sheng, and Q. Lu, npj Quantum Mater. **6**, 56 (2021).

[45] I. O. Troyanchuk, N. V. Kasper, D. D. Khalyavin, H. Szymczak, R. Szymczak, and M. Baran, Phys. Rev. Lett. **80**, 3380 (1998).

[46] J. L. Garcia-Munoz, J. Padilla-Pantoja, X. Torrelles, J. Blasco, J. Herrero-Martín, B. Bozzo, and J. A. Rodríguez-Velamazán, Phys. Rev. B **94**, 014411 (2016).

[47] M. Kriener, C. Zobel, A. Reichl, J. Baier, M. Cwik, K. Berggold, H. Kierspel, O. Zabara, A. Freimuth, and T. Lorenz, Phys. Rev. B **69**, 094417 (2004).

[48] Y. Okimoto, X. Peng, M. Tamura, T. Morita, K. Onda, T. Ishikawa, S. Koshihara, N. Todoroki, T. Kyomen, and M. Itoh, Phys. Rev. Lett. **103**, 027402 (2009).

[49] J. L. Garcia-Munoz, C. Frontera, A. J. Barón-González, S. Valencia, J. Blasco, R. Feyerherm, E. Dudzik, R. Abrudan, and F. Radu, Phys. Rev. B **84**, 045104 (2011).

[50] K. H. Kim, T. Qian, and Bog G. Kim, J. Appl. Phys. **102**, 033910 (2007).

[51] I. Fita, I. O. Troyanchuk, T. Zajarniuk, P. Iwanowski, A. Wisniewski, and R. Puzniak, Phys. Rev. B **98**, 214445 (2018).

[52] I. Fita, I. O. Troyanchuk, T. Zajarniuk, A. Wisniewski, and R. Puzniak, Phys. Rev. B **101**, 224433 (2020).

[53] M. Tanaka, Y. Katsuya, and A. Yamamoto, Rev. Sci. Instrum. **79**, 075106 (2008).

[54] M. Tanaka, Y. Katsuya, Y. Matsushita, and O. Sakata, J. Ceram. Soc. Jpn. **121**, 287 (2013).

[55] H. M. Rietveld, J. Appl. Cryst. **2**, 65 (1969).

[56] F. Izumi and T. Ikeda, Mater. Sci. Forum **321–324**, 198 (2000).

[57] L. Lutterotti, Nuclear Inst. Methods Phys. Res. B **268**, 334 (2010).

[58] K. Momma and F. Izumi, J. Appl. Crystallogr. **44**, 1272 (2011).

[59] R. Liu, R. Scatena, D. D. Khalyavin, R. D. Johnson, Y. Inaguma, M. Tanaka, Y. Matsushita, K. Yamaura, and A. A. Belik, Inorg. Chem. **59**, 9065 (2020).

[60] See Supplemental Material at http://link.aps.org/supplemental/10.1103/PhysRevB.106.104425 for the atomic positions, occupancies, and thermal displacement parameters of the structures

of GSCO and GCCO obtained using synchrotron XRD, temperature dependence of the lattice parameters, and volume of the orthorhombic unit cells of GSCO and GCCO.

[61] A. C. Komarek, T. Möller, M. Isobe, Y. Drees, H. Ulbrich, M. Azuma, M. T. Fernández-Díaz, A. Senyshyn, M. Hoelzel, G. André *et al.*, Phys. Rev. B **84**, 125114 (2011).

[62] F. Damay, C. Martin, V. Hardy, A. Maignan, G. André, K. Knight, S. R. Giblin, and L. C. Chapon, Phys. Rev. B **81**, 214405 (2010).

[63] H. L. Feng, M. Reehuis, P. Adler, Z. Hu, M. Nicklas, A. Hoser, S.-C. Weng, C. Felser, and M. Jansen, Phys. Rev. B **97**, 184407 (2018).

[64] A. B. Antunes, O. Peña, C. Moure, V. Gil, and G. André, J. Magn. Magn. Mater. **316**, e652 (2007).

[65] J. Blasco, J. L. García-Muñoz, J. García, G. Subías, J. Stankiewicz, J. A. Rodríguez-Velamazán, and C. Ritter, Phys. Rev. B **96**, 024409 (2017).

[66] M. K. Kim, J. Y. Moon, S. H. Oh, D. G. Oh, Y. J. Choi, and N. Lee, Sci Rep **9**, 5456 (2019).

[67] R. B. Griffiths, Phys. Rev. Lett. **23**, 17 (1969).

[68] C. He, M. A. Torija, J. Wu, J. W. Lynn, H. Zheng, J. F. Mitchell, and C. Leighton, Phys. Rev. B **76**, 014401 (2007).

[69] A. Haldar, K. G. Suresh, and A. K. Nigam, Europhys. Lett. **91**, 67006 (2010).

[70] M. Balanda, Acta Phys. Pol. A **124**, 964 (2013).

[71] K. Manna, A. K. Bera, M. Jain, S. Elizabeth, S. M. Yusuf, and P. S. Anil Kumar, Phys. Rev. B **91**, 224420 (2015).

[72] R. Kumar, P. Yanda, and A. Sundaresan, Phys. Rev. B **103**, 214427 (2021).

[73] R. Mathieu, P. Jönsson, D. N. H. Nam, and P. Nordblad, Phys. Rev. B **63**, 092401 (2001).

[74] B. Mali, H. S. Nair, T. W. Heitmann, H. Nhalil, D. Antonio, K. Gofryk, S. R. Bhandari, M. P. Ghimire, and S. Elizabeth, Phys. Rev. B **102**, 014418 (2020).

[75] A. E. Berkowitz and K. Takano, J. Magn. Magn. Mater. **200**, 552 (1999).

[76] J. Nogués, J. Sort, V. Langlais, V. Skumryev, S. Suriñach, J. S. Muñoz, and M. D. Baró, Phys. Rep. **422**, 65 (2005).

[77] M. Patra, M. Thakur, S. Majumdar, and S. Giri, J. Phys.: Condens. Matter **21**, 236004 (2009).

[78] I. Fita, V. Markovich, A. S. Moskvin, A. Wisniewski, R. Puzniak, P. Iwanowski, C. Martin, A. Maignan, R. E. Carbonio, M. U. Gutowska *et al.*, Phys. Rev. B **97**, 104416 (2018).

[79] J. Geshev, J. Appl. Phys. **105**, 066108 (2009).

[80] J. Nogués, D. Lederman, T. J. Moran, and I. K. Schuller, Phys. Rev. Lett. **76**, 4624 (1996).

[81] J. Nogués, C. Leighton, and I. K. Schuller, Phys. Rev. B **61**, 1315 (2000).

[82] D. Niebieskikwiat and M. B. Salamon, Phys. Rev. B **72**, 174422 (2005).

[83] J. Krishna Murthy and P. S. Anil Kumar, Sci. Rep. **7**, 6919 (2017).

[84] Y. Y. Jiao, Q. Cui, P. Shahi, N. N. Wang, N. Su, B. S. Wang, M. T. Fernández-Díaz, J. A. Alonso, and J. -G. Cheng, Phys. Rev. B **97**, 014426 (2018).

[85] D. A. Salamatin, N. Martin, V. A. Sidorov, N. M. Chtchelkatchev, M. V. Magnitskaya, A. E. Petrova, I. P. Zibrov, L. N. Fomicheva, J. Guo, C. Huang *et al.*, Phys. Rev. B **101**, 100406(R) (2020).

[86] J. Y. Moon, M. K. Kim, Y. J. Choi, and N. Lee, Sci. Rep. **7**, 16099 (2017).

[87] M. Das, P. Sarkar, and P. Mandal, Phys. Rev. B **101**, 144433 (2020).

[88] J. Y. Moon, M. K. Kim, D. G. Oh, J. H. Kim, H. J. Shin, Y. J. Choi, and N. Lee, Phys. Rev. B **98**, 174424 (2018).

[89] P. Mandal, V. S. Bhadram, Y. Sundarayya, C. Narayana, A. Sundaresan, and C. N. R. Rao, Phys. Rev. Lett. **107**, 137202 (2011).

[90] A. Shaw, A. Mitra, S. D. Kaushik, V. Siruguri, and P. K. Chakrabarti, J. Magn. Magn. Mater. **488**, 165338 (2019).

[91] M. Goto, T. Oguchi, and Y. Shimakawa, J. Am. Chem. Soc. **143**, 19207 (2021).